CHAPTER 5

Seismic Inversion Results

In this chapter, results from two different seismic inversion methods are presented: 1) a Model-Based Deterministic Inversion and 2) a Stochastic Gabor Inversion. The necessary procedures to invert the seismic volume can be summarized, as follows:

a) Log editing and seismic-to-well-tie, as already presented in Chapter 4. At this stage, we also estimate a final average wavelet to use in the deterministic inversion process. The stochastic Gabor inversion routine includes its own wavelet-extraction procedure;
b) Initial model of acoustic impedance (alternatively density and p-wave velocity as well) is built by interpolating well data throughout the seismic volume. This interpolation is guided by the interpreted seismic horizons (Chapter 3);
c) A pre-inversion analysis is carried out to estimate inversion parameters;
d) Acoustic impedance using model-based deterministic inversion is estimated by updating the initial model using the misfit function between the synthetic (which is the convolution of the initial model with the extracted wavelet) and the real seismic section. This procedure continues to get the minimum acceptable error. Since low frequencies from the initial model will be merged with the estimated AI from the seismic signal, the final inversion result will be given in absolute acoustic impedance values;
e) The stochastic Gabor inversion method is able to automatically extract the non-stationary properties of the source wavelet to obtain high-resolution reflectivity. The bias added by the initial model allows the conversion of seismic amplitudes into absolute acoustic impedance estimates

5.1. Low-Frequency Model (or Initial Model)

Seismic inversion requires a low-frequency model in order to obtain absolute impedance from a seismic trace (Francis, 2005). Without absolute AI estimates, it is not possible to obtain formation properties, such as bulk density and velocity. For that reason, the low-frequency model is so important – because it provides prior information (a constraint) that allows relative acoustic impedance estimates to be converted into absolute AI values.

Theoretically, the initial model is supposed to include information at lower frequencies than those contained in the seismic data. Geologically, it can be thought of as a general compaction trend (low-frequency), especially for clastic sedimentary layers, that is added into the inversion process. The seismic bandwidth over the inversion target normally is measured, so that the well log data can then be filtered accordingly. Normally, a low-pass filter is used for that purpose, assuring that the initial model includes only low frequencies that are absent from the seismic data.

The amplitude spectrum of the seismic cube over the interval from 200 ms above the shallowest part of the Moki Fm. to 200 ms below the deepest part of the Top-Mangahewa horizon shows a frequency range from approximately 14 to 52 Hz, with dominant frequency around 30 Hz (Figure 5.1). Thus, a low-pass filter (10/14 Hz) was applied to the well logs before interpolation. Well logs from four different wells were used to create the low-frequency model: Kea-1, Moki-1, Maui-4 and Whio-1. The reasons for the choice of these wells are: (1) they were drilled in four different structures, with two discoveries (Moki-1 and Maui-4) and two dry holes (Kea-1 and Whio-1); (2) it is the choice that provides approximately the best coverage – control points relatively well spread – considering the available wells (see Figure 1.5 or Figure 5.3); (3) all of these four wells penetrate not just the Moki Fm., but at least a significant part of the Mangahewa Fm., which are, respectively, the primary and secondary inversion targets; (4) similar phases are estimated from the four well ties (see Chapter 4) and were used to extract the final average wavelet used in the deterministic inversion.

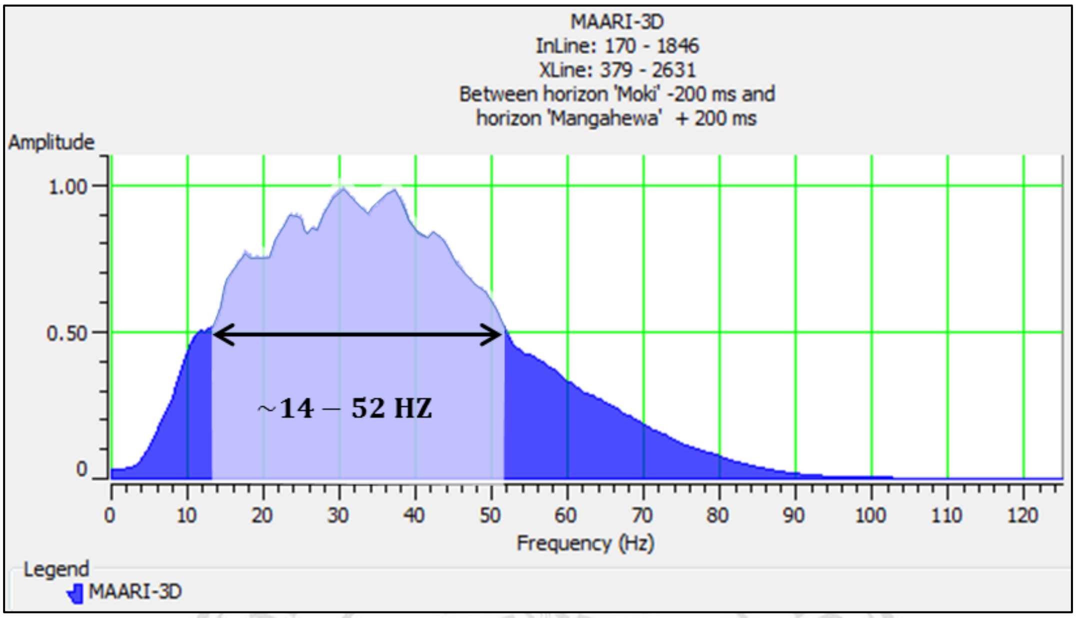

Figure 5.1: Amplitude spectrum of the Maari 3D seismic data extracted from the inversion target interval

A vertical section of the low-frequency model (XL 1644) through the Maari-1 well – which was not included in the model – shows a fairly good match between interpolated acoustic impedance values and acoustic impedance at the well location (Figure 5.2a). It also goes through the Moki-1 well. Along the well paths, both colors and curves represent the computed acoustic impedances at the well locations. The frequencies of the displayed well data and the low-frequency model are different, though. The well data is filtered (high-cut: 50-60 Hz) and the initial model has frequencies up to 14 Hz. The Hampson-Russell software creates initial models for bulk density and P-wave velocity along with the P-Impedance model (Figures 5.2b and 5.2c). These show the low-frequency models for these two properties along cross-line 1645. The models are constrained by phantom horizons 400 ms above Moki (top) and 400 ms below the Mangahewa horizon (bottom).

An arbitrary line (A-B) was created through all available wells, so we can see how the low-frequency (P-Impedance) model varies between the well control points (Figure 5.3). It is clear there are lateral variations within a one stratum. The Moki Fm., for example, has low AI values at the wells Moki-1, Maari-1 and Maari-2 and in the upper part of the formation in the Maui-4 well on the Manaia structure. High AI values are seen in Kea-1 well, Moki-2A, Whio-1 and in the lower part of the formation at Maui-4. The interpolation balances these values between the wells. Note how the high AI values (light blue color, ~9300 ((m/s)*(g/cc))) gradually change into medium to low values (red and yellow colors, ~7000-8000 ((m/s)*(g/cc))) at the central part, influenced by the Moki-1 well log data. Between the lower Manganui and the Mangahewa horizon the model is pretty consistent. It presents high to very high AI values at the Kea-1 location. The ideal would be to map other events (Otaraoa, Tikorangi and Taimana formations) in this interval to better constraint the initial model. Due to the poor quality of the seismic data, however, these events were found to be highly discontinuous and consequently any interpretation would have poor accuracy (as the lower Manganui had) and time-consuming.

The Maari-2 well is the only well that has high AI values above the Moki horizon and do not match with the created model. In the Moki-2A well, high AI values occur in the sampled section of the Moki Fm. and also do not match with the model. Lateral property variations do occur in nature, especially in structurally complex areas such as the Southern Taranaki Basin. Another interesting zone is found in the deepest part of the central area. A last few samples of the Moki-1 well represent a decrease in AI and these values are then projected further down and interpolated laterally until they fade into high AI values coming from the Maui-4 well data. As Maui-4 was actually sampled along that entire interval, the low AI zone below Moki-1 is more likely to be a mathematical interpolation artifact than a geological low-frequency response of that zone.

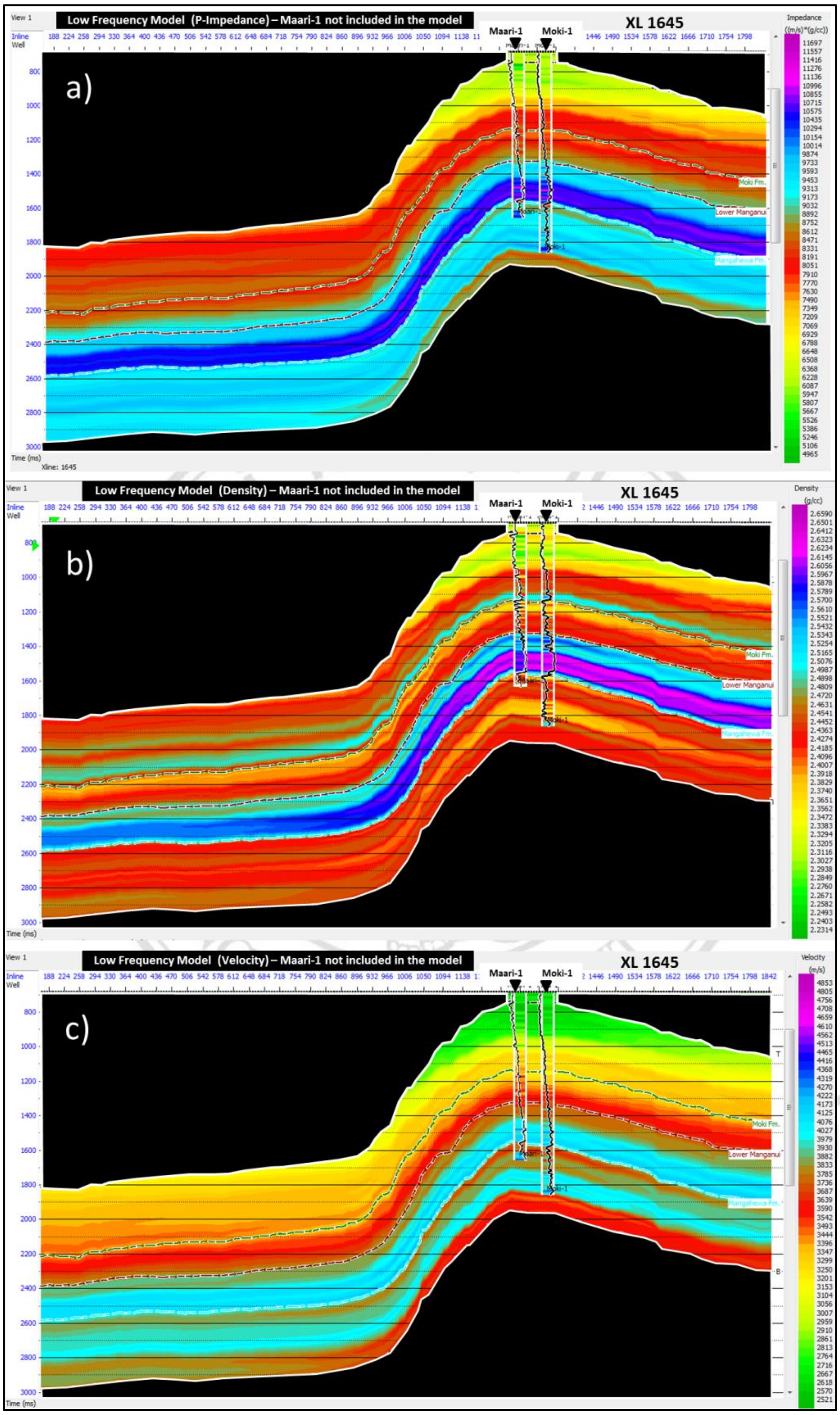

Figure 5.2: Low-Frequency models created for a) P-Impedance, b) bulk density and c) P-wave velocity. These models are exhibited along a vertical section (XL 1645) that passes through the wells Maari-1 (not included in the model) and Moki-1. For each model shown, the color display and curves correspond to the respective property at the well locations

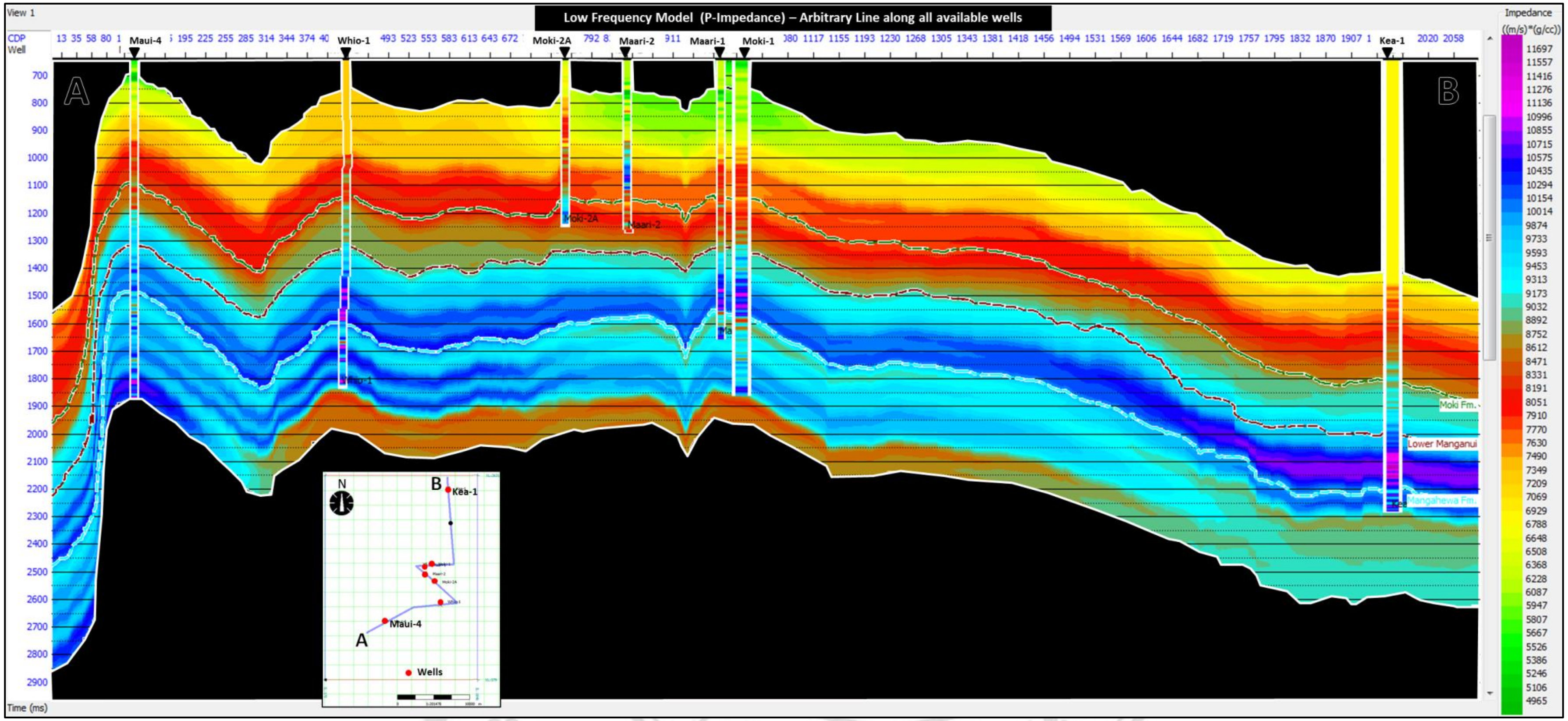

Figure 5.3: Low-Frequency model of P-Impedance ((m/s)*(g/cc)) along an arbitrary line (A-B) through all available wells in the area. Well locations and the arbitrary line segment on a map view are also shown

5.2. Model-based Deterministic Inversion Analysis

An inversion analysis is performed to define the ideal parameters for inverting the seismic data. The deterministic inversion was run on the Hampson-Russell software, which allows the user to compare inverted and real acoustic impedance curves, correlate between the forward-modeling result and actual seismic data, calculate Root-Mean-Square (RMS) error, etc. The wells included in the inversion process were Moki-1, Maui-4, Maari-1 and Kea-1. The inversion used a hard constraint setting the maximum deviation to be within $\pm$50% of the acoustic impedance log values. The average block defines the thickness in milliseconds for the initial layers of the model and was set to be 1 ms. A pre-whitening of 1% was chosen to stabilize the inversion procedure. This value is a default from the Hampson-Russell software that does not accept values of less than 1%. A total of 10 iterations was chosen. The number of iterations has an interesting effect on the inversion analysis. A high number of iterations increases the RMS error between inverted trace and computed acoustic impedance trace along the well locations, but improves the correlation between the synthetic and the actual seismic trace. A low number of iterations has the opposite effect. For example, with 10 iterations, in the Maui-4 well, the RMS impedance error between the inverted and original AI curve was 630 (m/s*g/cc) and the cross-correlation between the synthetic and actual trace is 0.988 with RMS error equal to 15%. Increasing the number of iterations to 50, the RMS impedance error between the inverted and original AI curve increased to 720 m/s*g/cc and the cross-correlation between the synthetic and actual trace is 0.997 with RMS error equal to 8%. So, due to this trade-off, iterations were set to 15 to improve the convergence while keeping errors between the inverted and original impedance log less than 10% of the AI values range.

The inversion analysis from the Kea-1 well is shown in Figure 5.4. The ‘Zp’ column shows the low-frequency model trend (black), original AI log (blue) and inverted AI (red curve). At Kea-1, the RMS error of 422 m/s*g/cc between the inverted trace and original AI curve corresponds to less than 5% of the range of AI values – approximately 6000-13000 m/s*g/cc – along the target interval, but is comparable to a typical change in impedance from layer to layer. The final average wavelet (see Figure 4.19) used in the process is shown, as well as the synthetic trace (from the AI inversion) and the actual seismic trace and their cross-correlation and RMS error. The inversion analyses for the other wells included in the inversion are shown in Appendix A.

Inverted and original acoustic impedance data are plotted in Figure 5.5. A zone constraint was used to show only the data points between the upper Manganui and Farewell markers. The RMS error is 339 m/s*g/cc. The z-axis (colored data points) indicates that, in general, P-Impedance increases linearly with depth (or time in TWTT), as expected due to compaction effects. There are, however, data points from ~1500 ms (purple) that present anomalous P-Impedance values in the range of 7500-8000 m/s*g/cc when the expected for this time zone (TWTT) are values above 10000 m/s*g/cc, as illustrated in Figure 5.5.

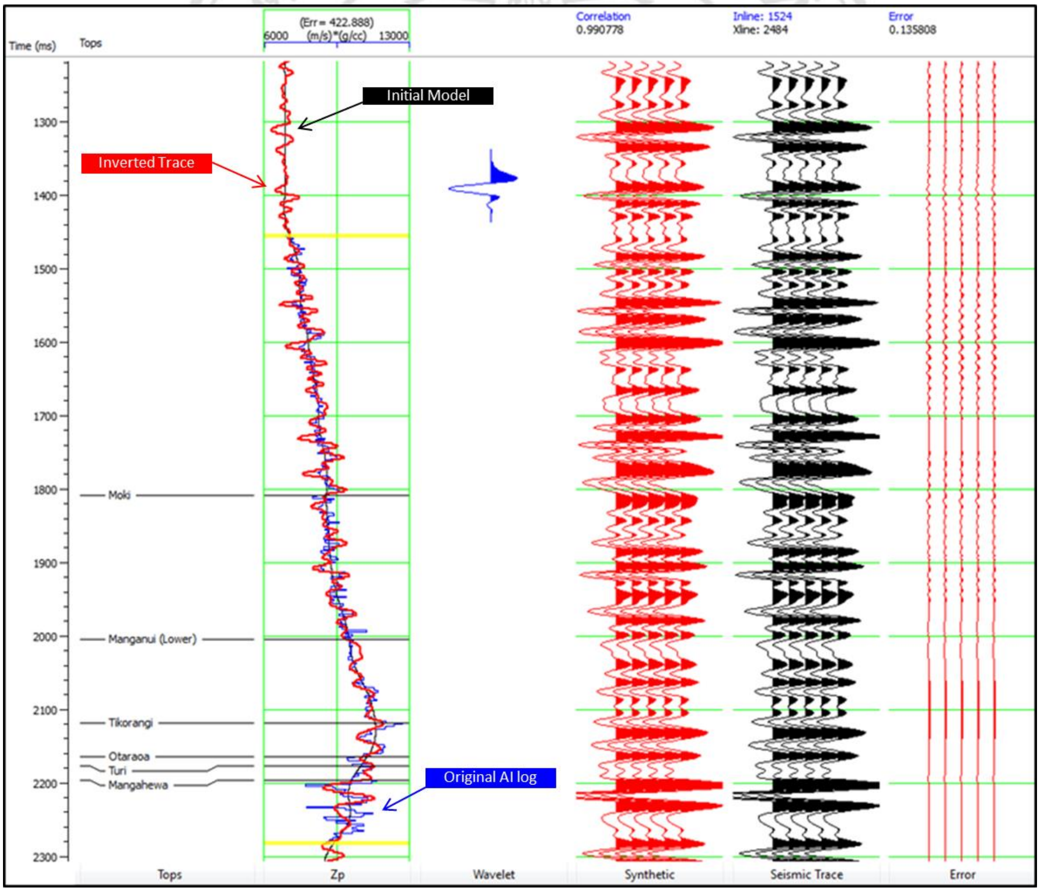

Figure 5.4: Acoustic-impedance inversion analysis at Kea-1. The final average wavelet was extracted from four different wells (see Figure 4.18)

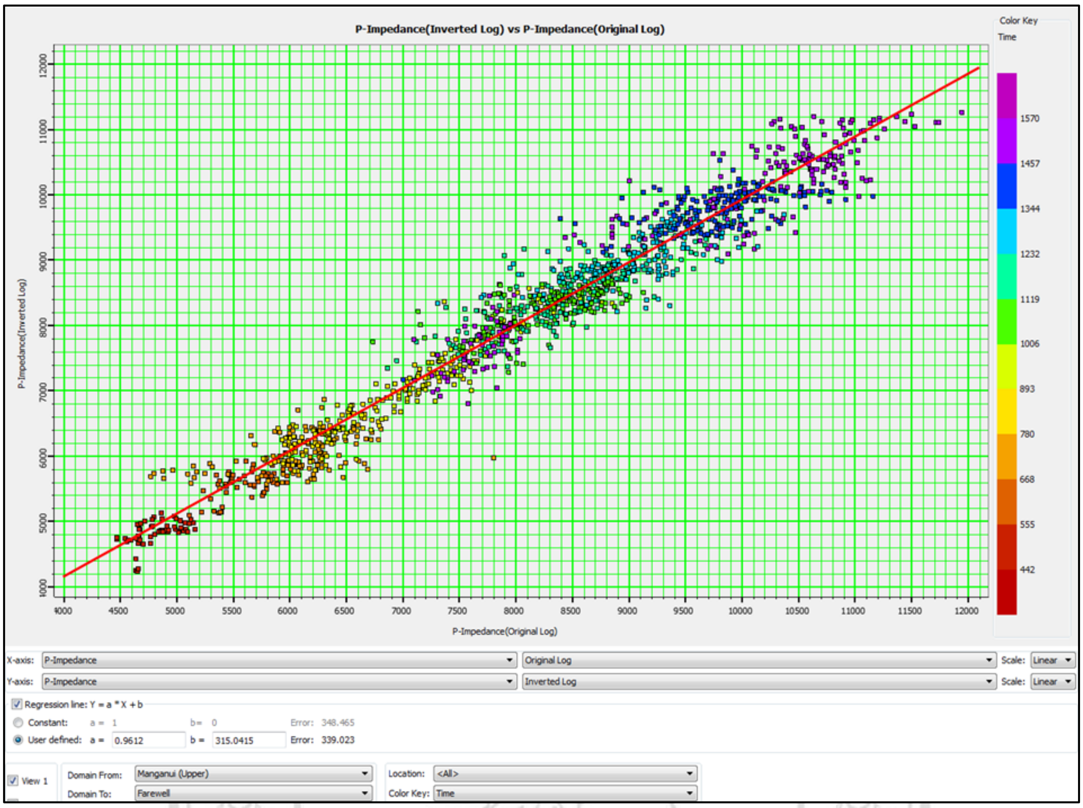

Figure 5.5: Inverted P-Impedance (y-axis) and original P-Impedance data (x-axis) show some scatter (RMS error of $\pm$340 m/s*g/cc) from the ideal line y = x. Data are colored by two-way travel time (TWTT) in milliseconds

5.3. Deterministic Inversion Results

The model-based deterministic inversion aims to minimize the error between the forward convolution of the reflectivity from an estimated impedance profile and the seismic amplitudes, at every trace of the seismic volume. The constraint provided by the initial low-frequency model makes it possible to obtain absolute acoustic impedance values. This inversion method was applied to the full-stack Maari seismic data between the interval defined by two phantom horizons. The upper bound is 400 ms above the Top Moki horizon and the lower bound is 400 ms below the Mangahewa horizon (Figure 5.6). The interval includes the main reservoir – sandstones of the Moki Fm. – and the secondary target, the Mangahewa Fm., an older unit within the Kapuni Group. The thin sands within the upper Manganui formation, formally known as M2A sands, are also included. The wavelet used to invert the data is an average wavelet extracted from the wells Kea-1, Maui-4, Moki-1 and Whio-1, with an average phase of 123° and dominant frequency around 26 Hz (see Section 4.2.1). The prior information required to obtain absolute P-impedance results was provided by the initial low-frequency model described and presented in Section 5.1. The inversion parameters are described in Section 5.2. Four wells were included in the inversion procedure: Kea-1, Maui-4, Moki-1 and Maari-1. The inverted seismic cube was evaluated using blind wells. This method consists of leaving out one or more wells originally included in the inversion process and then inverting the data again to measure the mis-tie with the AI in the left-out well.

P-Impedance from Model-based Deterministic inversion is shown along an arbitrary line (Arbitrary Line A-B, see Figure 5.3 for location) crossing all the available wells (Figure 5.6). The seismic data along the same arbitrary line is presented in Figure 5.7. Computed AI (original) curve at the well locations is displayed over the P-Impedance section. The inverted P-impedance range is approximately 6400 to 10300 (m/s*g/cc) along the arbitrary line. High acoustic impedance values are seen between the Lower Manganui horizon and the Mangahewa horizon. This interval includes other formations from the Ngatoro Group: Otaraoa, Tikorangi and Taimana. This group is marked by highly calcareous sediments. The Tikorangi Fm. is a bioclastic limestone and the Manganui Fm. is mainly mudstones and siltstones. Due the geology, high values are really expected in this interval. Within the Moki Fm., there are variations. Low AI values are mainly seen around the wells Moki-1, Maari-1 and Maari-2, in the Moki-Maari structure. The Moki-1 well completion report says hydrocarbons were found within the first sands of the Moki unit. The interval is divided in three pay zones (1306-1343 m MD BKB). Zone 1 is 10 m thick with average porosity of 23.3%; zone two is 7.3 m thick with porosity of 19%; and zone 3 is 7 m thick, avg. porosity values ~18%.The AI values within the Moki Fm. range from ~7500 to 9400 m/s*g/cc.

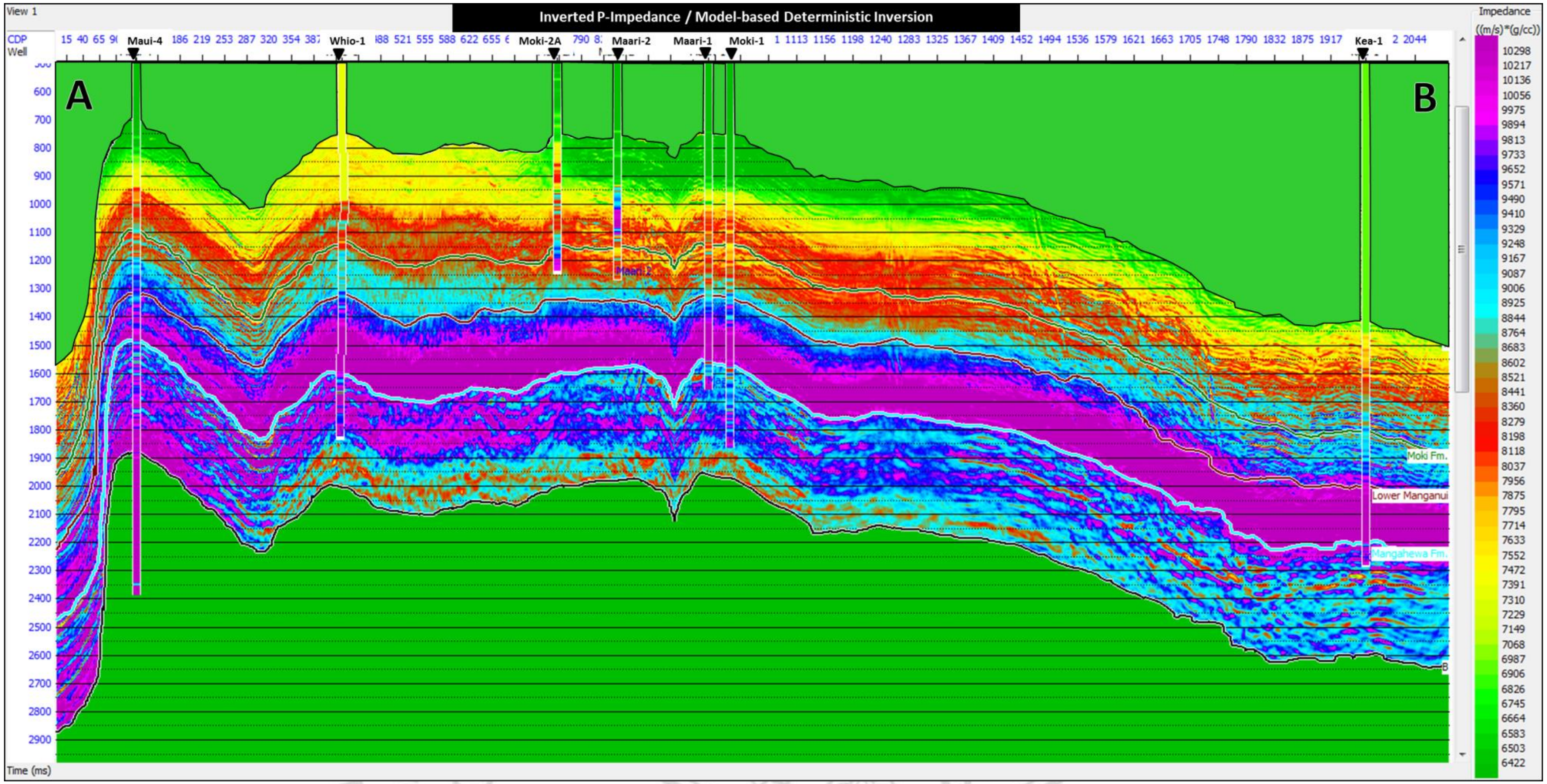

Figure 5.6: P-Impedance along an arbitrary line (A-B). The volume was obtained from a model-based deterministic inversion. Well AI values are displayed using the same color bar as the inversion. Wells included in the inversion process match well the inverted AI. Computed AI in the Whio-1 well, which was not included, matches the inverted result quite well. At the Maari-2, which also was not included, the match is just moderate. At Moki-2A, where the seismic data is quite poor, the inversion is not reliable

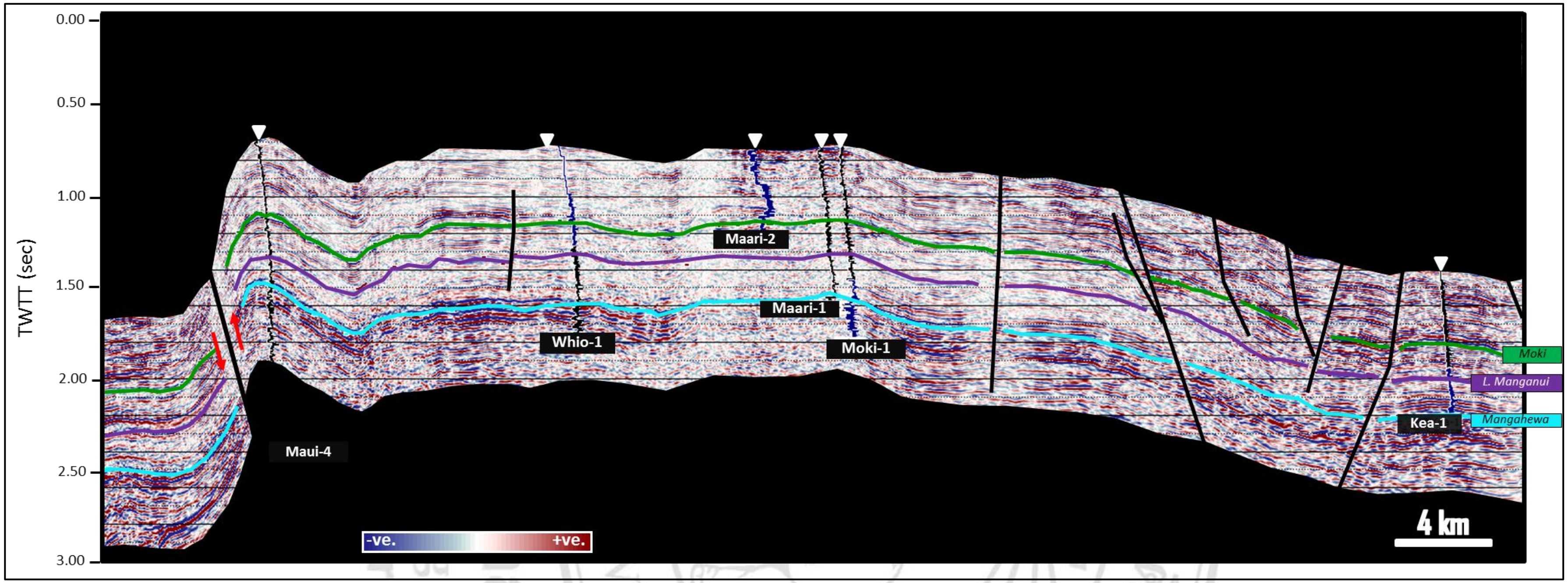

Figure 5.7: Arbitrary seismic line through all the wells (except Moki-2A) in the inversion target zone. P-velocity logs are displayed at the wells

The wells Whio-1 and Maari-2 were left out of the inversion procedure. As seen in Figure 5.6, inverted AI matches well the acoustic impedance log at Whio-1. At Maari-2 well, the match is poor above the Moki horizon, with the Maari-2 well showing higher acoustic impedance (above 9500 m/s*g/cc, blue and purple color) than any other available well in the interval between 1000-1100 ms TWT. One difference between these wells is that Whio-1 was used to create the low-frequency model used in the model-based inversion, whilst the Maari-2 well was not. Due to the limited number of available wells in most of the inversion projects, the initial model carries a lot of uncertainty about the truly general compaction trend (low-frequency component of the acoustic impedance log).

We inverted the seismic data again, this time with the wells Maari-1 and Kea-1 left as blind-wells, so we could assess the accuracy of the seismic inversion results. One can say the results are reliable if the wells left out (or blind-wells) match the inversion results. Figures 5.8, 5.9 and 5.10 show the match between inverted AI and well-log AI for the following blind wells: deviated Whio-1 well (1^{st} inversion run); Maari-1 and Maari-2 (2^{nd} inversion run) and Kea-1 well (2^{nd} inversion run).

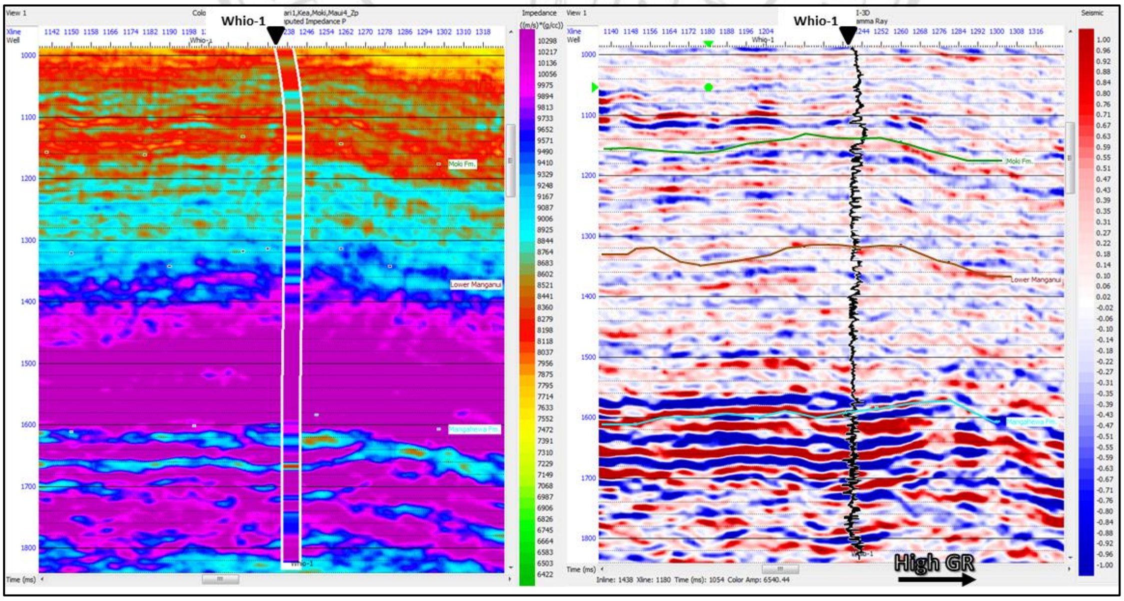

Figure 5.8: Whio-1 well as a blind well in the 1^{st} inversion run. The inverted P-Impedance (left) matches the computed AI well. Gamma-Ray log is shown over the seismic section (right), IL 1438

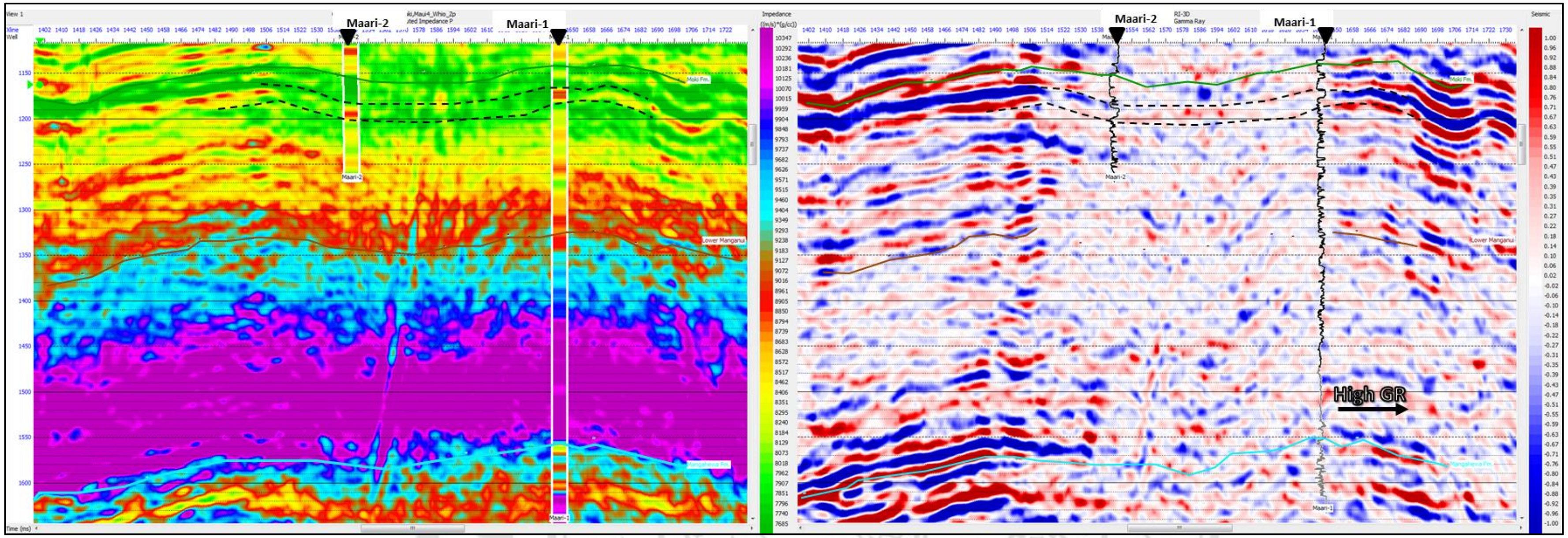

Figure 5.9: Maari-1 and Maari-2 as blind wells. Inverted P-Impedance matches log AI well below the Moki horizon (left). The Gamma-Ray log is displayed over the seismic section (right), IL 1270. Note the imaging issue (attenuated amplitudes) occurring between the wells. This affects the inversion. In this case, it could lead to a misleading interpretation that all the interval between approximately 1130 and 1220 ms TWT has very low acoustic impedance. It seems more likely, though, that the imaging issue created a discontinuous shale interval (black dashed lines - higher acoustic impedance, high GR) that can be correlated between the two wells

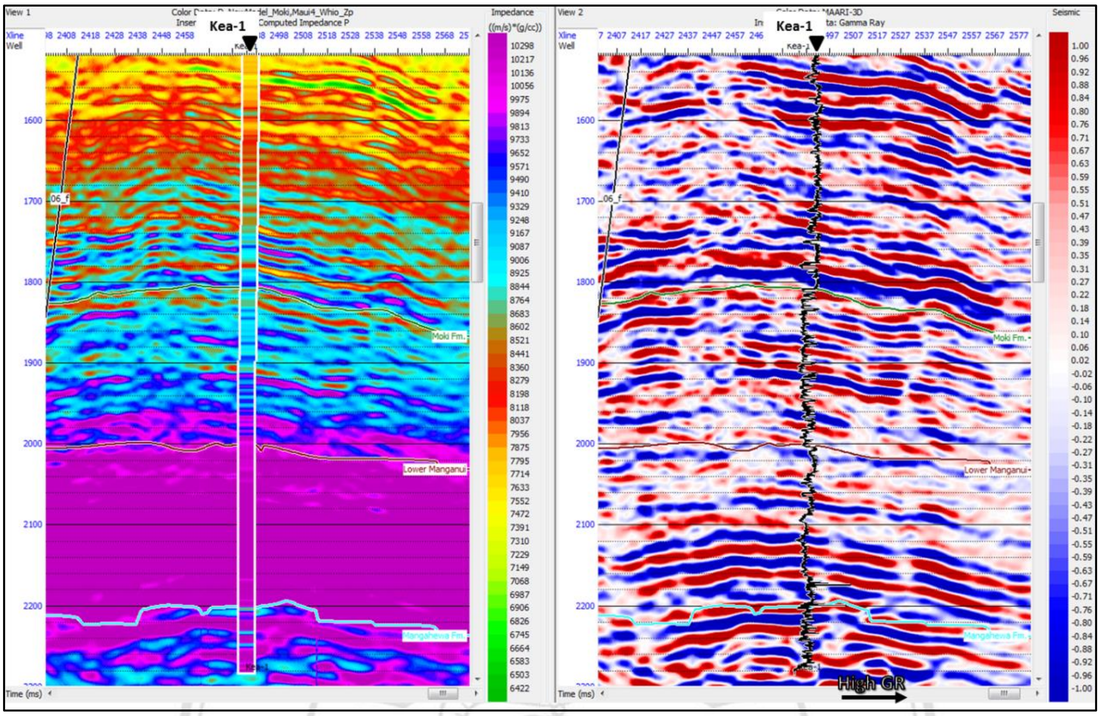

Figure 5.10: Kea-1 as a blind well in the 2nd inversion run. The inverted P-Impedance (left) matches the computed AI fairly well. The Gamma-Ray log is shown over the seismic section (right), IL 1524

5.4. Stochastic Gabor Inversion

By applying deterministic methods, the inversion results are merely an averaging function of the solution (Oldenburg *et al.*, 1983). The limited bandwidth of the wavelet and the intrinsic noise prevent us from getting back the true reflectivity function, i.e., a series of spikes that represent the actual geological signature. Moreover, wavelet estimation is affected by the quality of the seismic and well data. Low signal-to-noise ratios will prevent us from extracting correct wavelets and that will be incorporated into deterministic inversion results (Naghadeh *et al.*, 2017). The stochastic Gabor Inversion surpasses these restrictions by considering the non-stationary nature of the seismic signal. The method has the ability to extract time-variant wavelets using the Gabor transform approach introduced by Margrave *et al.* (2003). By removing most of the source wavelet effect, the obtained reflectivity will have higher frequency content. Prior information coming from the well logs are added and will draw the inverted stochastic Gabor result to be very close to the real acoustic impedance.

A full description of the parameters used to run the Stochastic Gabor inversion (Naghadeh *et al.*, 2017) is given below:

- The stochastic Gabor algorithm automatically extracts the time-variant wavelet properties from a signal confined in a window of length l by applying a Hilbert transform to the logarithm of its amplitude spectrum. A window of 500 milliseconds was used. This window is shifted down sample by sample so that if a trace has n samples, n wavelets are extracted;
- The low-frequency information comes from the same initial model used in the model-based deterministic inversion (Figure 5-3). The model included frequencies up to 14 Hz and considered the well logs from the wells Kea-1, Moki-1, Maui-4 and Whio-1;
- A geostatistical model containing high frequencies was created from the well-log data. The model uses a function that rapidly decays as the distance from the well locations increases. At the well locations the well data has a weight of 20% on the inversion result and this influence decreases with distance to a minimum weight of 1%. We thereby force the seismic data to have the most influence away from the wells. Since the objective function in the stochastic inversion is a weighted combination of the misfit function and the model penalty function, increasing bias from the well logs at the well location means decreasing bias from the seismic data and vice-versa. Getting more bias from the well logs sacrifices the seismic data, which is not desired.

The time-variant wavelet properties are compiled into a Kernel Matrix to be deconvolved with the seismic data in the time domain. This matrix brings the data to zero-phase and enhances the temporal resolution by effectively removing the source wavelet effects. Computationally, this matrix is heavy. The time to compute one realisation on the full-offset stacked volume did not meet the planned timeframe of this project. Measures had to be taken, and a viable solution was to increase Inline and Xline bin spacing by a factor of two. Thus, Inline and Xline bin spacing became 50m and 25m, respectively. It reduced the original .SEGY file from around 22 GB to 5.5 GB. Still, the time to compute a single realization was over 48 hours. That limits the method and prohibits any chance of estimating uncertainty in large seismic files due the elevated number of realizations required.

The stochastic Gabor inversion was applied to the Maari seismic data. Three inverted property volumes were obtained: P-Impedance, Bulk Density and P-wave velocity. Figure 5.11 presents the results from the three inverted volumes in detail along XL 1643. The line passes through wells Moki-1 and Maari-1, which is useful to analyze the match between the inversion result and well data along wells from which bias was taken (Moki-1) and the ones that were not considered (Maari-1). Maari-1 is approximately 800 m west of Moki-1. The color ribbons displayed at each well correspond to the respective inverted property being shown. At each well, the GR log is also shown (black curve). The Inverted P-Impedance is presented along an arbitrary line (Figure 5.13) and that way it can be directly compared to the deterministic inversion shown in Figure 5.6.

The enhanced resolution provided by the stochastic Gabor method is evident. Considering the dominant frequency of the seismic data in the Moki Fm. ~30 Hz and an average P-wave velocity value of 2500 m/s (see Session 4.3), the minimum resolvable thickness, solely by the seismic data, is approximately 20 meters (1/4 of a wavelength). Sequences of shales with interbedded sands within the Manganui unit are differentiated by the P-Impedance inversion result. Shales normally have higher density and higher velocity than sandstones. With depth, though, sands are compacted, lose porosity and we may not be able to differentiate these lithologies through acoustic impedance anymore. Within the Moki Fm. – our main inversion target – that goes from 1140 to 1320 ms TWT depth in Figure 5.11, shales and sands seem to be fairly well distinguishable by P-impedance (Figures 2.21 and 2.24). In this interval, along XL 1643, sandstones have a range of AI values around 7000-7700 m/s*g/cc and shales around 8800-9400 m/s*g/cc. The lithologies are indicated by the GR log, with sands having low GR values and shales having high GR values.

The inversion results present a fairly good match with the computed AI and with the density and p-wave velocity logs along the wells – even though just a 20% weight is assigned to the original logs at the well location. The color ribbon shows the property corresponding to each inversion in its original frequency. The three inverted property volumes provide high-resolution geologic information. Cross-plots of inverted AI with the additional inverted volumes density and P-velocity will be tested for a lithology classification scheme using the LithoSI module from Hampson-Russell software.

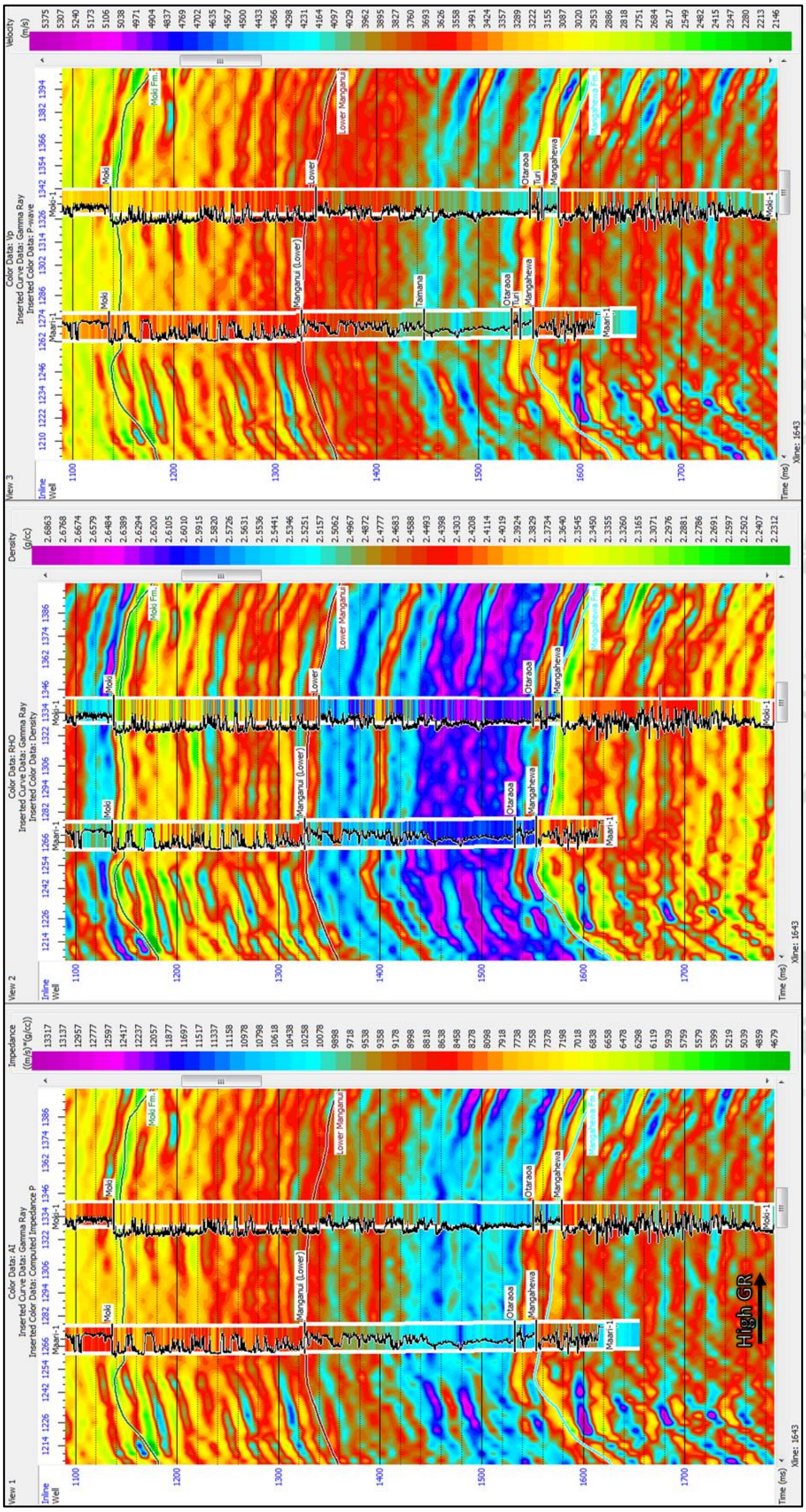

Figure 5.11: Inversion on XL 1643 from the stochastic Gabor method showing the properties P-Impedance (left), density (middle) and P-wave velocity (right)

A similar phenomenon to what was observed in the deterministic inversion between the Maari-1 and Maari-2 (Figure 5.9) also occurs in Figure 5.11. The seismic section between the Maari-1 and Moki-1 wells is marked by attenuated amplitudes. The amplitudes cause discontinuities in what is likely to be continuous layers and it is observed in all three inversions. Figure 5.12 shows the seismic section along the same line as shown in Figure 5.11, where we see the zone of attenuated amplitudes. The cause of this attenuation is not clear. A bright event seen at the top of structure (750 ms TWT) could be a cause of this energy attenuation, but the amplitude dimming is seen just at one side of this bright reflector. This also could be related to some N-S trending fault that is poorly imaged due the seismic acquisition direction.

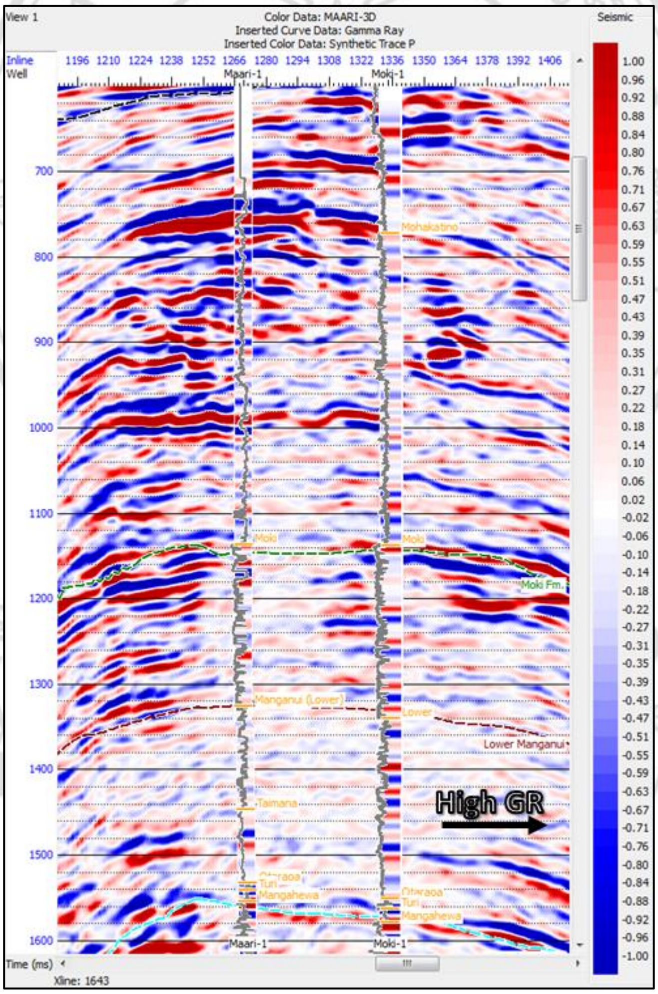

Figure 5.12: Detailed view of the zone with attenuated amplitudes between Maari-1 and Moki-1 on XL 1643. The color ribbon at each well shows the computed synthetic seismogram and the gray curve is the GR log

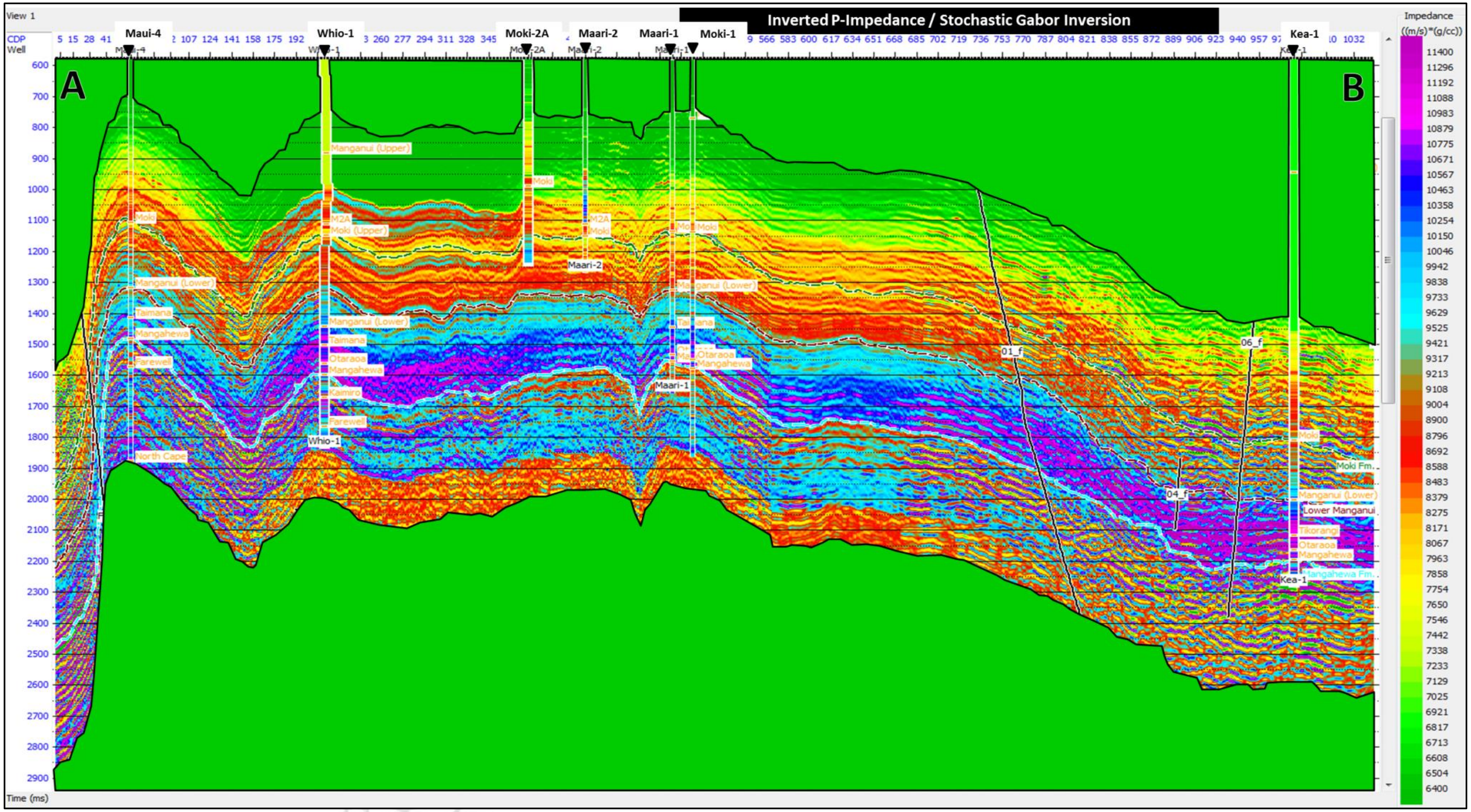

Figure 5-13: Inverted P-Impedance along an arbitrary line (A-B). The volume was obtained from the Stochastic Gabor Inversion. Computed AI values are displayed on a color-match display at the well locations

5.5. Time and Stratal Slices

A series of time and stratal slices were taken to assess the distribution of acoustic impedance in the Maari area. Figure 5.16 shows the inverted P-Impedance (arithmetic mean) from the upper 16 ms of the Moki Fm. (search window of 16 ms below Top Moki horizon) from the stochastic Gabor (a) and deterministic (b) inversions. It also shows the seismic amplitudes along the Moki horizon (c) and top of Moki Fm. time-structure map (d). This target zone was defined based on the Moki-1 well-logs as shown in Figure 5.14. Two pay zones are mentioned by de Bock *et al.* (1991) in the intervals 1306-1316 and 1317-1326 m MD below KB and that are highlighted by a green rectangle, approximately from 1138-1154 ms TWT. At this depth, overlying shales have higher acoustic impedance than the underlying sands that we are trying to map.

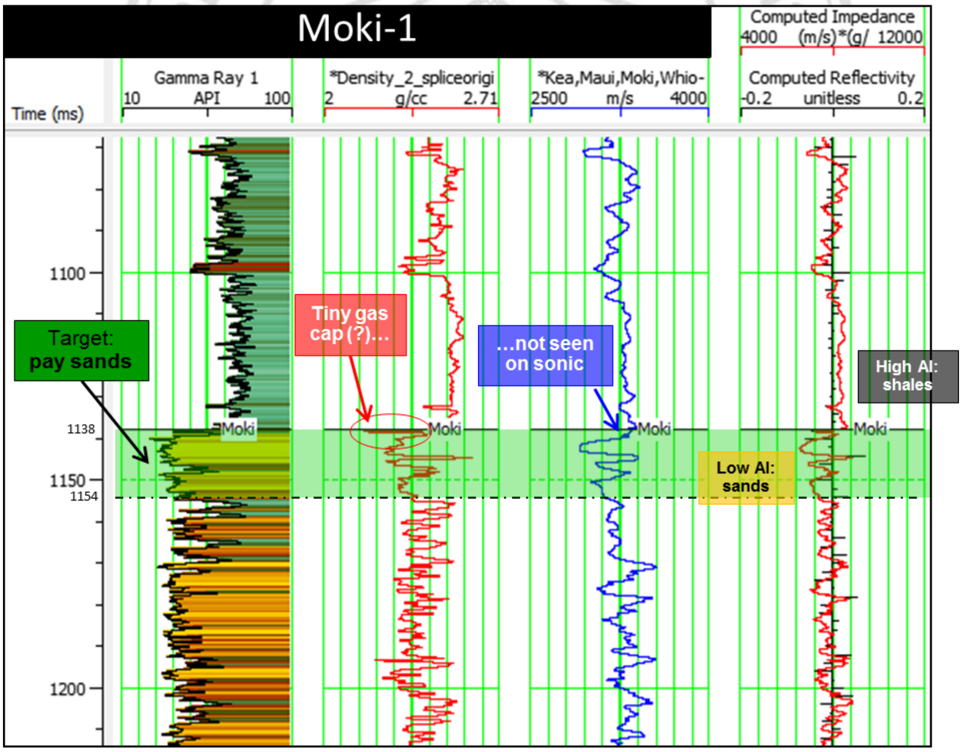

Figure 5.14: Target zone for the stratal-slice shown in Figure 4.15: two hydrocarbon pay intervals separated by a 1 meter shale layer in the upper part of the Moki Fm. (de Bock *et al.*, 1991)

The second inversion target is the Eocene Mangahewa formation (Kapuni Group). Oil was found within the sands of the Mangahewa Fm. still in 1970 by the exploration well Maui-4 in the interval 2031-2073 m MD below KB or 1482-1502 ms TWT (Figure 4.15). The well-log quality in this interval is a concern. Caliper log indicates the presence of a wash-out zone in the Turi Fm. The question is whether it has significantly affected the density log or not. This is important once we want to differentiate shales (overlying lithology, Turi Fm.) from the Mangahewa sands by using the inverted acoustic impedance. The current scenario shows lower densities and higher P-wave velocities in the Turi Fm. compared to the Mangahewa sands. The result is a low contrast of computed AI between both formations, especially at the upper 5 ms of the Mangahewa unit (Figure 5.15). Figure 5.17 shows the inverted P-Impedance (arithmetic mean) from the upper 20 ms of the Mangahewa Fm. from the stochastic Gabor (a) and deterministic (b) inversions. Seismic amplitudes along the interpreted Mangahewa horizon (c) and time-structure map (d) are also shown.

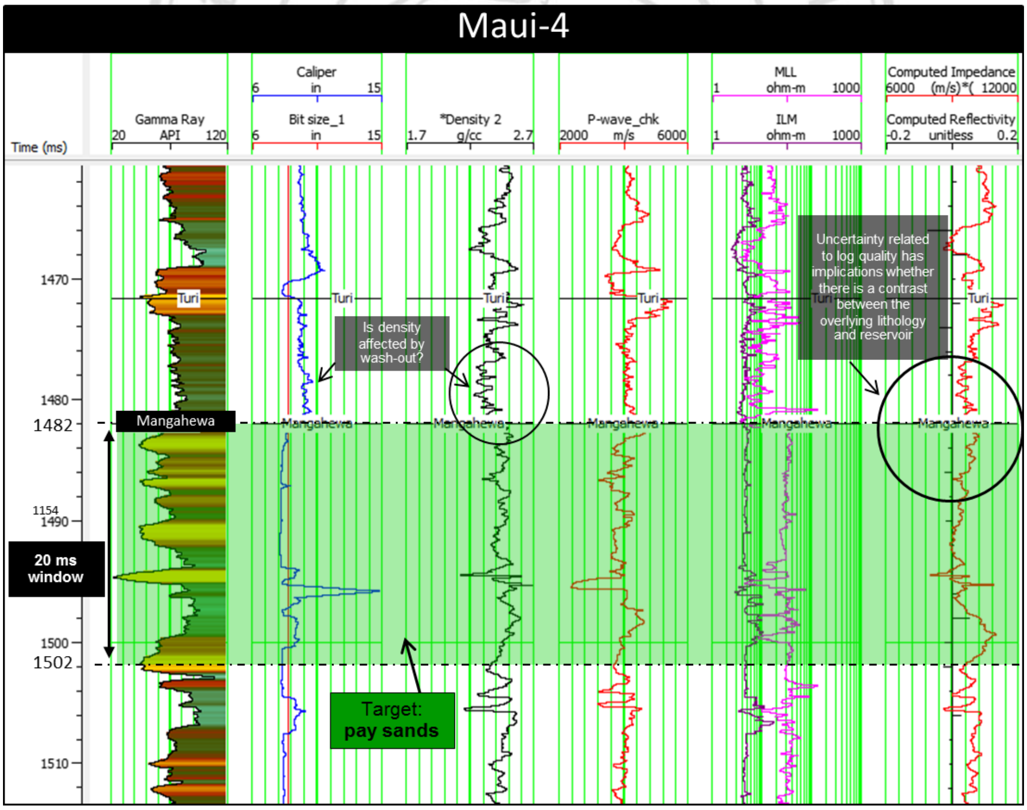

Figure 5.15: Target zone for the stratal-slice shown in Figure 5.17 is the interval 2031-2073 m MD below KB that corresponds to approximately to the upper 20 ms within the Eocene Mangahewa formation

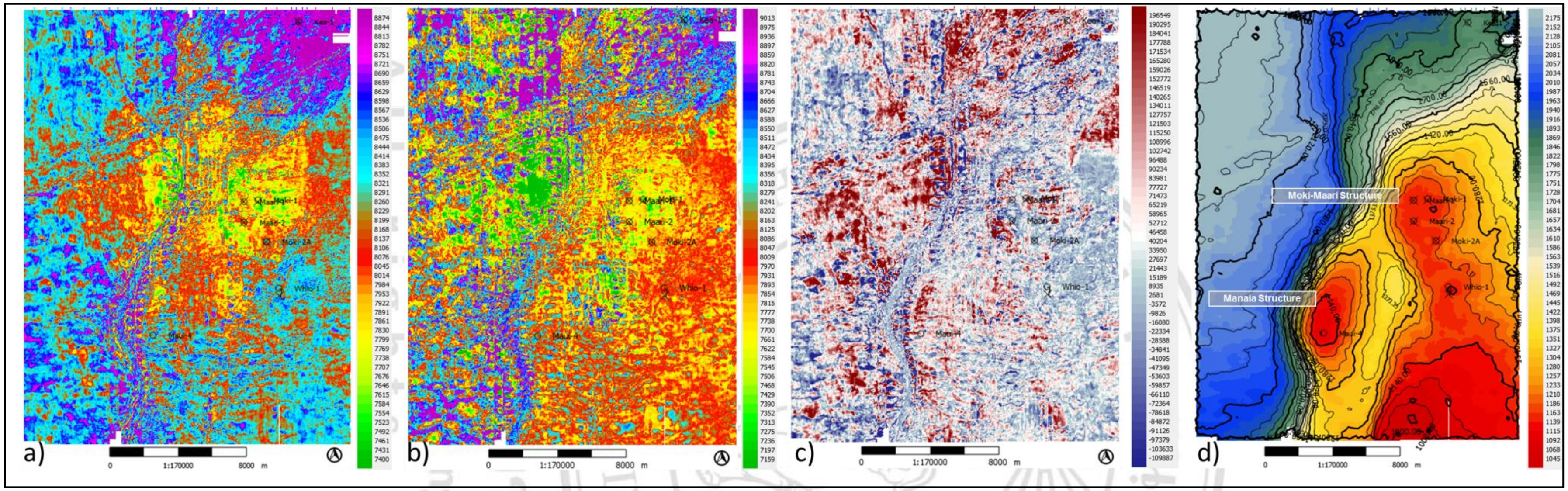

Figure 5.16: Inverted P-Impedance (m/s*g/cc) from deterministic inversion (a), (b) from Stochastic Gabor inversion in the upper 16 ms of the Moki Fm. Seismic amplitudes along the Moki horizon (c) and its time-structure map (d) are also shown

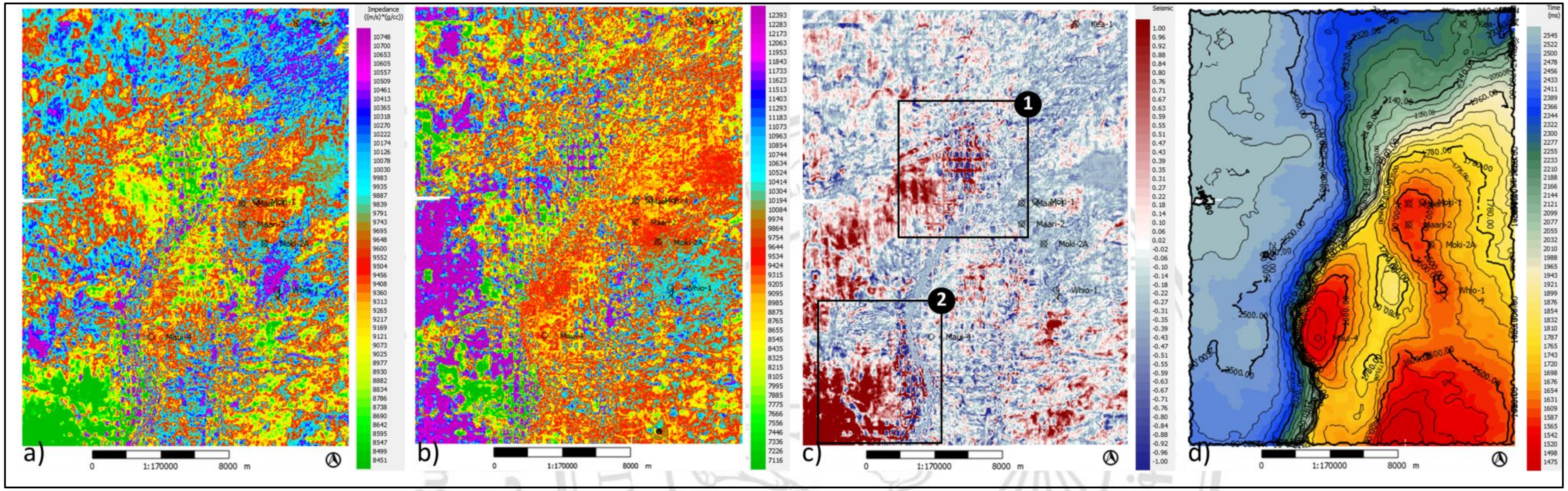

Figure 5.17: Inverted P-Impedance (m/s*g/cc) from deterministic inversion (a), (b) from Stochastic Gabor inversion in the upper 20 ms of the Mangahewa Fm. Seismic amplitudes along the top Mangahewa horizon (c) and its time-structure map (d) are also shown

Figure 5-16 shows different stratal-slices results from the deterministic and stochastic Gabor inversion in a pay interval (upper 16ms) of the Moki Fm. Deterministic (a) shows a well-defined low AI zone at both sides of the major reverse fault in the central part of the map, where the upthrown hanging wall forms the Moki-Maari structure. The stochastic Gabor shows low impedance values in the same zone, the difference is that low to medium values (7400-8100 m/s*g/cc) are extended further east and south. Near the crest of the Moki-Maari anticline (d), inverted AI values range from 7200-7800 m/s*g/cc. Three considerations have to be made, though: 1) the two maps have different range of acoustic impedance: 7400-8875 m/s*g/cc for deterministic (a), and 7160-9015 m/s*g/cc for stochastic Gabor inversion; 2) due to the higher frequencies in the stochastic Gabor volume, depending on the size of the search window, we may end up obtaining an average of two or more distinguished events; and 3) lateral resolution is not the same since bin size (for both Inline and Xline) in b) has double the size of a) (Session 5.4). The accuracy of the horizon picking is also a concern. The stratal-slice taken along the seismic volume (c), no search window used, shows the amplitude variation along the interpreted Top Moki horizon. The event was picked on a peak (positive amplitudes), but many negative values are seen in that map. As discussed in Chapter 3, the quality of the seismic data makes interpretation difficult for any event below the Plio-Pleistocene Unconformity. The use of a search window helps to minimize the uncertainty related to the interpretation, but some of that uncertainty is still dragged into the quantitative interpretation.

Figure 5.17 shows lateral AI variations along the upper 20 ms of the Mangahewa formation. The interval is described in the well completion report (Maui-4 in the Manaia structure) as a pay zone. Low to Moderate AI values (8500-9500 m/s*g/cc) are seen associated to the Manaia structure, the Moki-Maari structure, in the south-west (footwall of the major fault) and also in the south-eastern sector. Especially in this map, the range of the stochastic Gabor inversion (b) is significantly larger than the deterministic; many values are clipped in the map, especially in the western sector. Inverted AI values in the Manaia structure vary from 8700-9500 m/s*g/cc in the deterministic inversion (a) and from approximately 8500-9600 m/s*g/cc in the stochastic Gabor inversion (b). At this depth, extracted seismic amplitudes map along the Top Mangahewa horizon shows linear events occurring around the major fault that are likely to be processing fingerprints (rectangles 1 and 2 in Figure 5.17c). Figure 5.18 shows these areas in detail. These linear features are also observed in the deterministic and stochastic Gabor inversion results.

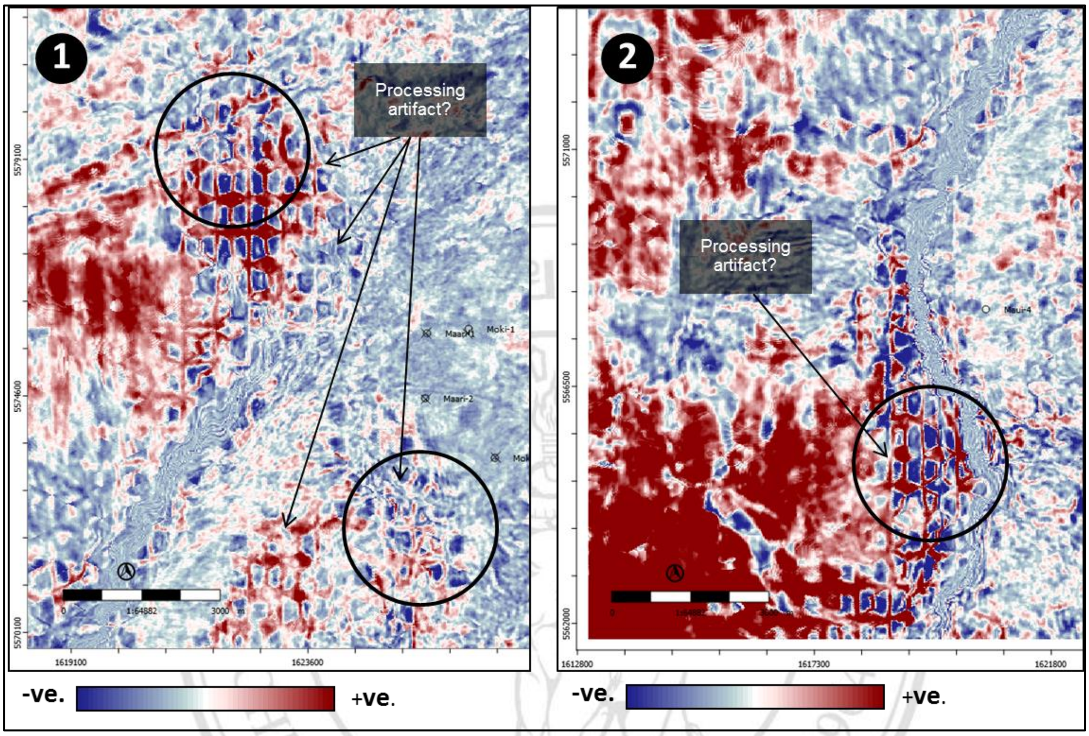

Figure 5.18: Detailed view of the highlighted areas 1 and 2 in Figure 5.17. The extracted amplitude map (stratal slice) along the Top Mangahewa horizons shows these linear features, possible processing artifacts, in the seismic data

Time-slices were also used to observe inverted AI distribution with time. Figures 5.19 and 5.20 exhibit time-slices at 1200ms and 1800 ms taken from three different data volumes: a) P-Impedance Deterministic inversion; b) P-Impedance stochastic Gabor inversion; and c) seismic data. This is also a way to quality-check the inversion results. We expect the inversion results to be similar with the seismic data in some aspects, i.e., follow the same trend of reflection events in the time-slice, delineate structures, etc.

In both figures, the seismic data can be divided in two zones: one at the western part (foot-wall) of the major fault trending SSW-NNE and another at the eastern sector of this fault (hanging-wall). These areas contain different reflection trends and, overall, different amplitudes as well. The footwall of the major inverted fault is marked by strong events (high amplitude values). In the eastern zone, many zones present dim amplitudes. These zones are highlighted at 1200 ms in Figure 5-19c. Note how the anticline structures are well delineated both in all slices of Figure 5-19. It is clear that the stochastic Gabor inversion shows more details about the subsurface (P-Impedance changes that are related to lithology/fluid changes). A region is selected in Figure 5.20 and a detailed view at each map (Areas 1, 2 and 3) is exhibited in Figure 5.21.

Two potential advantages of the stochastic Gabor inversion are observed in Figure 5.21: enhanced resolution and amplitude recovery. Zone ‘a’ is marked by attenuated amplitudes (?), causing a discontinuity in reflection events, while zone ‘b’ shows an area where amplitudes seem to be preserved. Note how different are the deterministic (1) and stochastic Gabor (2) inversion at these zones. In ‘b’, stochastic inversion is able to distinguish events where deterministic shows a single high acoustic impedance zone. The change in acoustic impedance shown at that zone by the stochastic inversion coincides with the zero crossings in seismic. In ‘a’, the stochastic improves the continuity of attenuated reflection events, which is one advantage of non-stationary methods (Gabor)

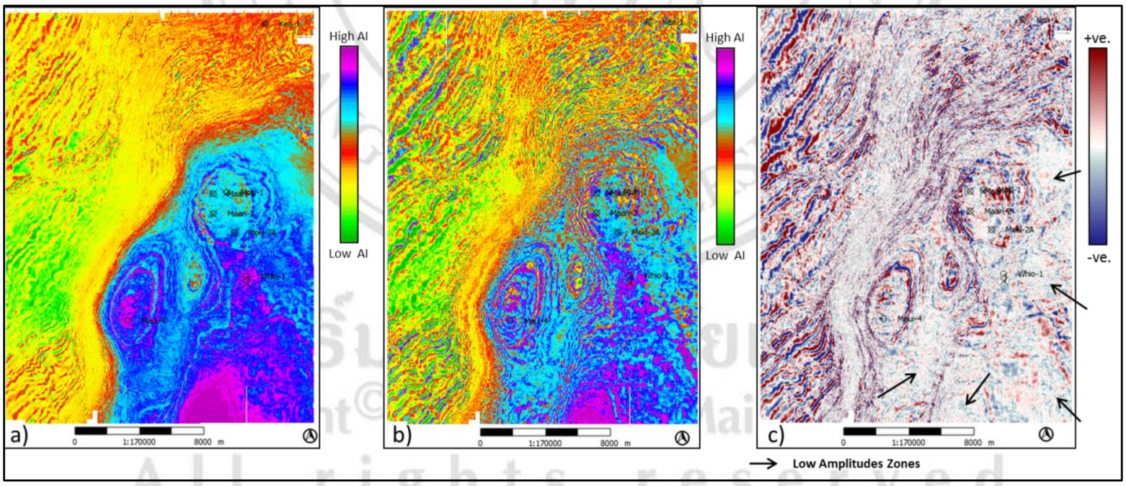

Figure 5.19: Time-slice at 1200 ms: a) P-impedance deterministic inversion, b) P-impedance stochastic Gabor inversion and c) seismic data

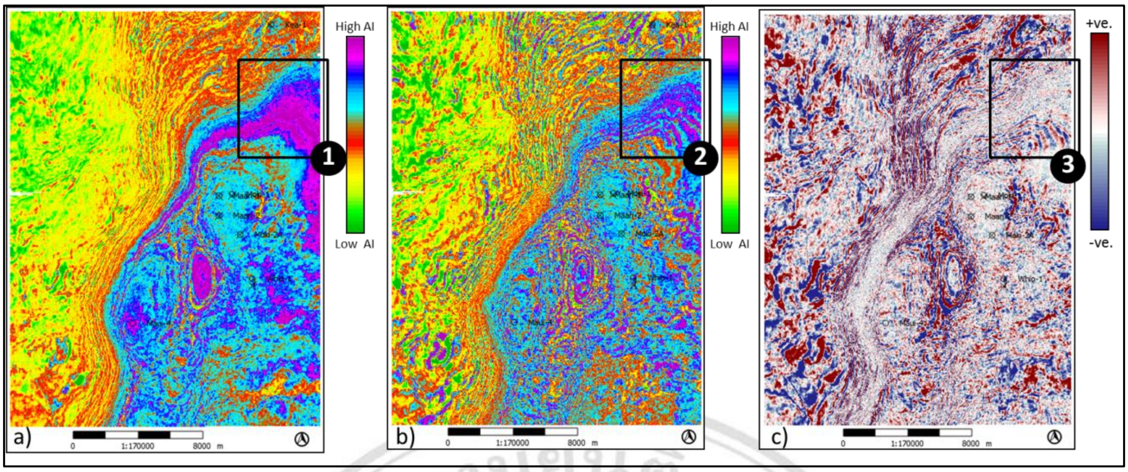

Figure 5.20: Time-slice at 1800 ms: a) P-impedance deterministic inversion, b) P-impedance stochastic Gabor inversion and c) seismic data

5.5. Lithology Prediction (LithoSI)

The different inverted volumes, i.e., P-impedance, density, P-wave velocity (Figure 5.11) can be used in a lithology classification scheme. Hampson-Russell software has a specific module to do that, referred to as LithoSI. Conditional probabilities and priori probabilities (well-logs) for a certain number of classes being classified are obtained through a Bayesian classification (Doyen, 2007). This classification scheme does not have to assume a normal distribution, once it uses a non-parametric estimation method – the kernel estimation (Hampson-Russel, 2015). The kernel estimation uses a function to assign different weights to nearby observations. Based on the two attributes (x and y) of the N observations analyzed, a joint density function is created to define proportions of how close a random sample is to x_0 and y_0 (Avseth *et al.*, 2010).

Ideally, P-Impedance or Elastic Impedance is analyzed against P-to-S velocity ratio, Poisson's ratio or the Lamé parameters, as it provides more information (better separation) about lithology and fluid changes. Maari 3D is only available as a full-stack, though. So, P-impedance and density volumes will be used for classifying lithologies in the Maari field. A lithology log (Figure 5.23) is created from a logged P-impedance *vs.* density based on three selected zones: sands, shales and sandy shales/shaly sands (Figure 5.22). Wells Maari-1, Maari-2, Maui-4 and Moki-1 were used, all oil wells.

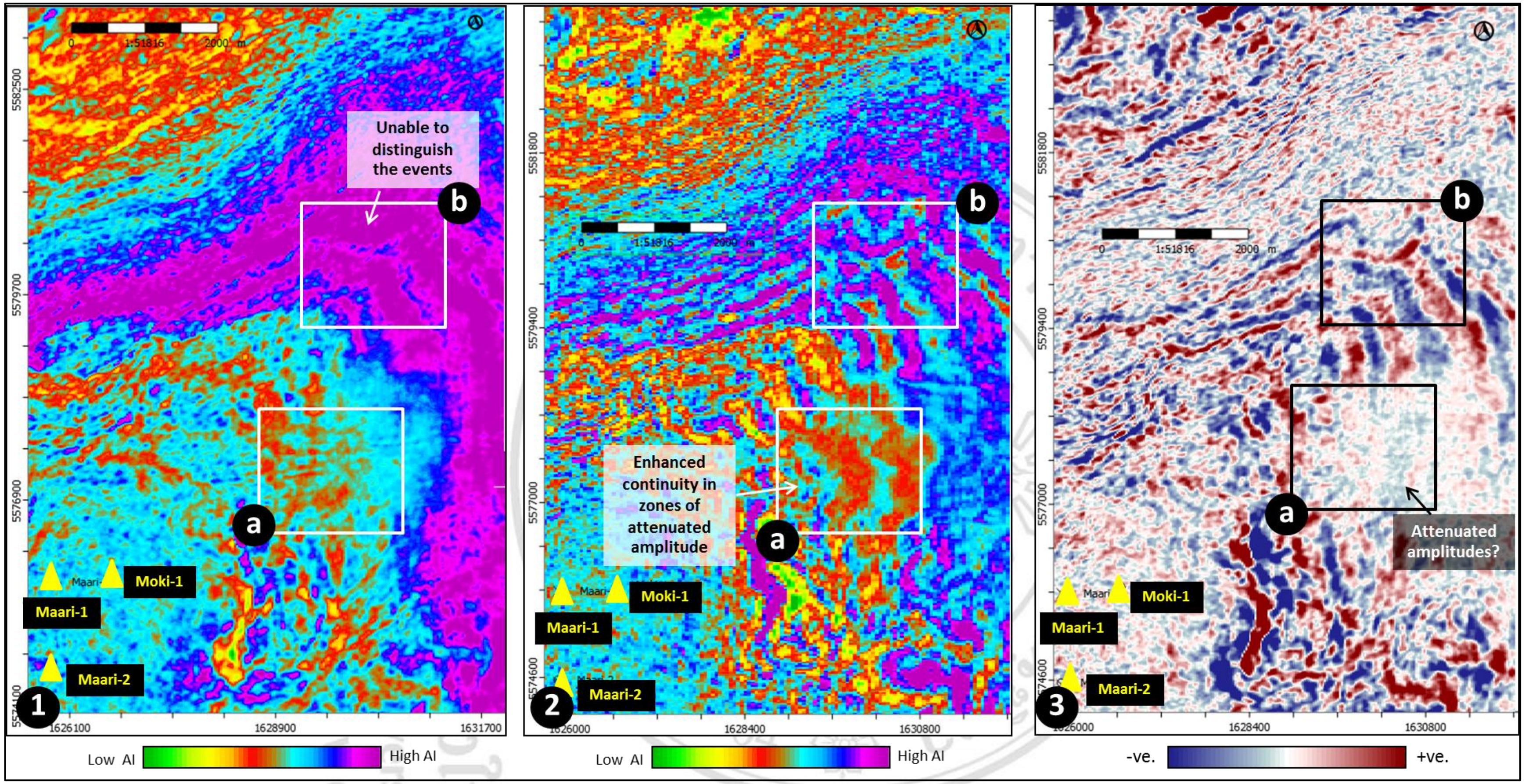

Figure 5.21: Detailed view of a selected area in Figure 5.20 showing (1) deterministic inversion, (2) stochastic Gabor inversion and (3) seismic amplitudes in a time-slice at 1800 milliseconds. Highlighted areas a) and b) show enhanced resolution and higher continuity of events in areas with damaged amplitudes given by the stochastic Gabor inversion

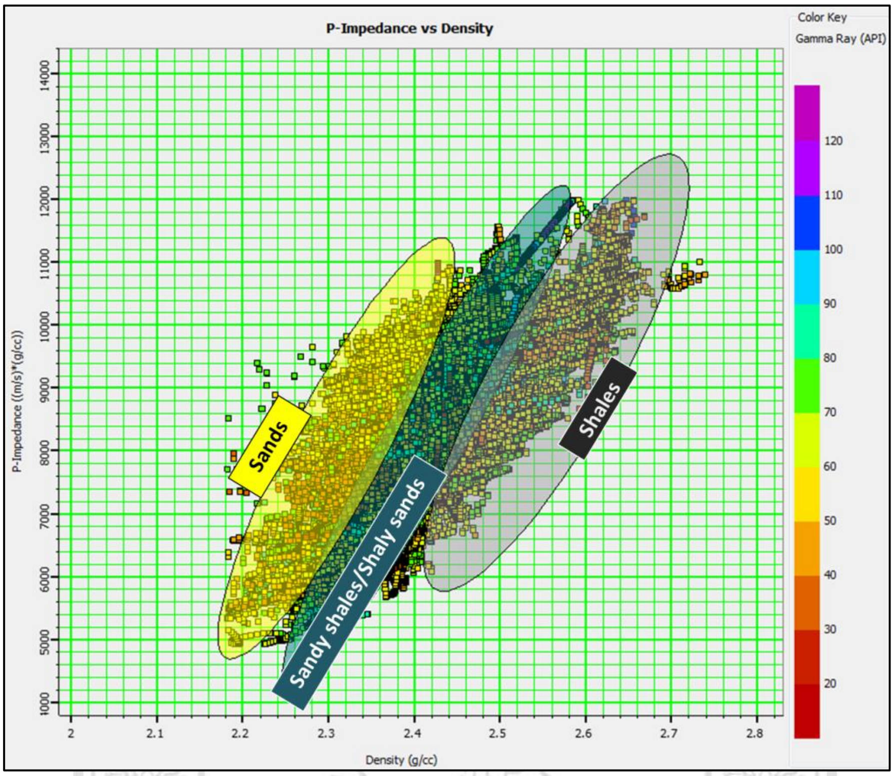

Figure 5.22: P-Impedance vs. density cross-plot from logged data using only wells Maari-1, Maari-2, Maui-4 and Moki-1. All sample points belong to the Moki formation

The selected areas in the cross-plot are used to produce the lithology logs at each well. In Figure 5.23 they can be checked against the GR log from each well. Another way of assessing the performance of the classifier is to use a confusion matrix, where the diagonal elements give the classification success rates for each litho-class (Doyen, 2007). The success rates will depend on how much overlap there is between each of the classes in their probabilistic density function (PDF). Figures 5.24 and 5.25 show the kernel matrix, with the PDF's for each class, and a summary of the confusion matrix for all the four wells used. Low success ratio values are associated to the class "Sands" when analyzed against the inversion volumes around the wells. That is caused by the overlapped area between the "Sands" and "Sandy hales/Shaly sands" PDF's attributes in the kernel matrix (Figure 4.24). After quality-checking the produced lithology logs and the classification success rates of each class, PDF's are used to produce probability maps for each one of the defined litho-classes.

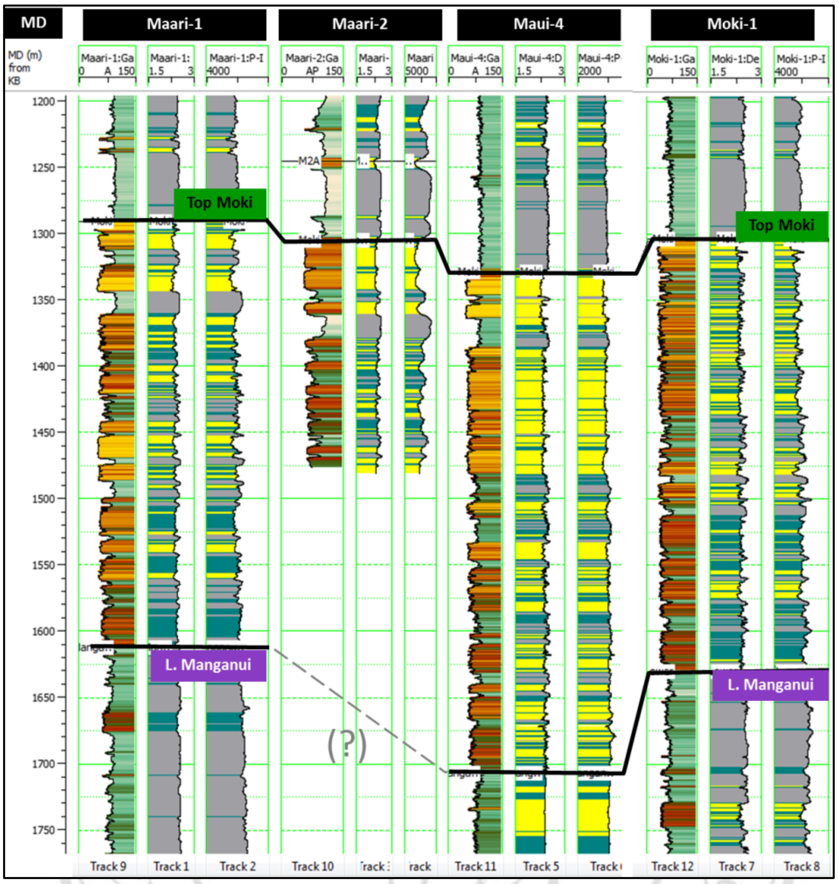

Figure 5.23: Selected zones from cross-plot shown in Figure 5.22 compared to the GR logs. At each well, tracks show GR (left), density log (middle) and P-Impedance (right)

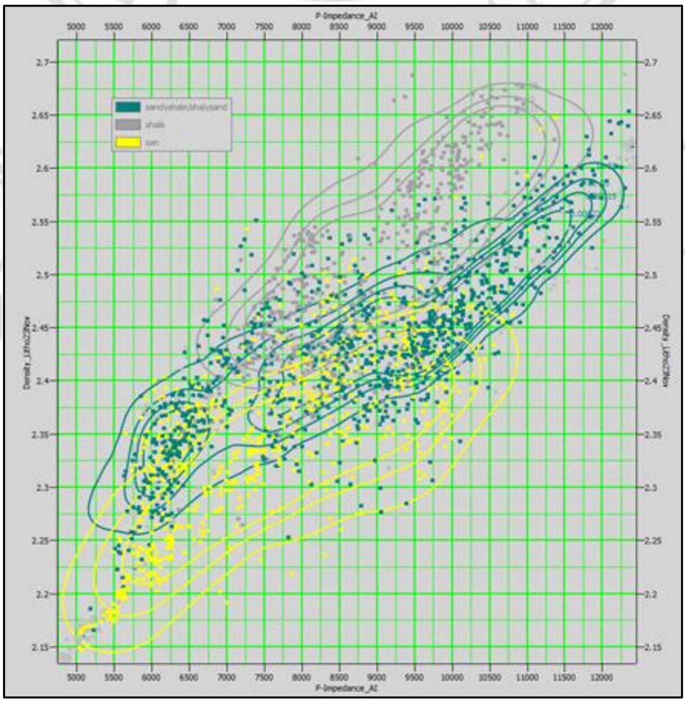

Figure 5.24: Computed Kernel matrix showing the PDF’s for each class

Well

Classification Success rates

Classified log

	sandyshale/shalysand	shale	san	Number of samples
sandyshale/shalysand	96.77%	0.62%	2.61%	32859
shale	3.91%	96.09%	0.00%	19775
san	13.66%	0.00%	86.34%	16828

a)

Volume traces extracted at well location

Classification Success rates

Classified log

	sandyshale/shalysand	shale	san	Number of samples
sandyshale/shalysand	75.68%	13.43%	10.89%	1258
shale	29.80%	66.29%	3.91%	537
san	43.68%	6.41%	49.92%	593

b)

Figure 5.25: Confusion matrix indicating the classification success rates of the selected zones (Figure 5.22) considering the well data (a) and the inversion volumes (b)

Stratal-slices were used to investigate the probability sands along two different intervals in the Moki formation. The first interval is described in the Moki-1 well completion report as a pay zone (1306.1 - 1316.8 m MD below KB). A search window of 8 ms below the Top Moki horizon was used to extract average probabilities of finding sands in this interval (Figure 5.26a). The second interval used a phantom horizon 50 ms below the top of the Moki Fm. and used a 5 ms centered window (phantom horizon ±2.5 ms) to extract sand probabilities.

In Figure 5.26a, high probabilities of sands occur around the Moki anticline – which was expected once the completion report points it a pay sand interval. The interesting is to see how these sands extend laterally. For the interval extracted, over 90% chances occur in the Moki structure in an area with approximately 2 km radius and pretty conformable with the structure. In Figure 5.26b, probabilities decrease around the Moki-1 well (~50-60%) and increase in the Manaia structure. An area with over 80% sand probabilities is seen around the Maui-4 well presenting a NW-SE trend – ~1.5 km wide and 3-4 kilometers long.

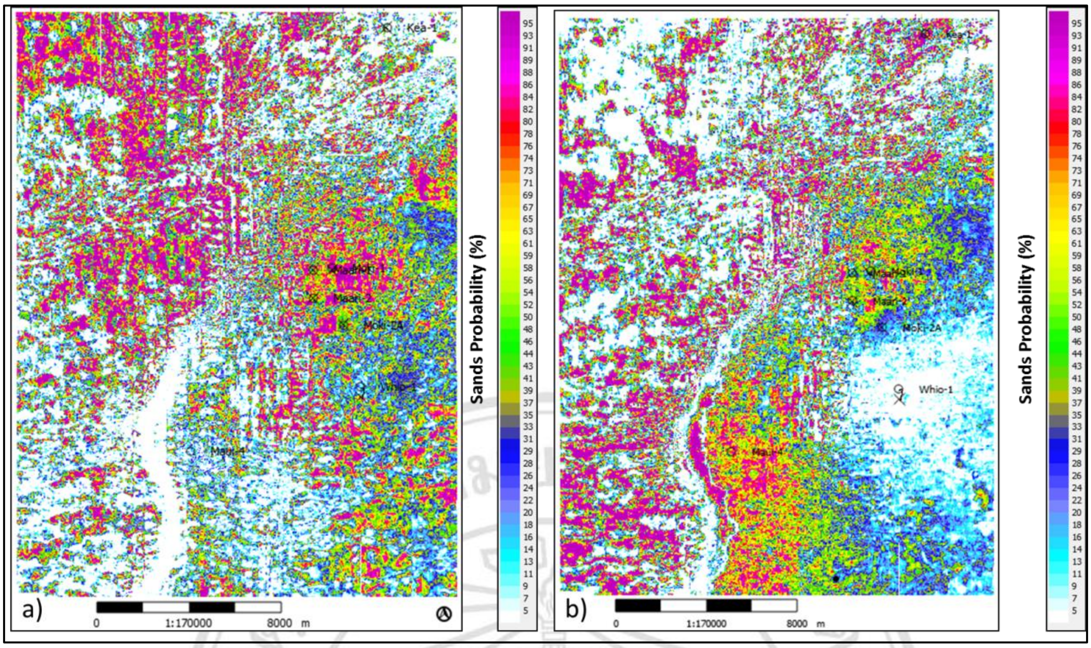

Figure 5.26: Sand class probabilities extracted from two different intervals: a) pay zone at Moki-1 well, 1306-1317 m MD. A search window of 8 ms was used to extract an average probability within the interval; b) phantom horizon (Moki horizon + 50 ms) with a search window of 5 ms centered in the phantom horizon

5.6. Porosity Prediction

By combining the inversion with the well information, it is possible to predict porosity (effective porosity) throughout the Maari field. Porosity (ϕ) is an important property of the reservoir. It is defined as a percentage of the total void space in a volume of rock. Effective Porosity (ϕ_{eff}) only accounts for interconnected spaces, i.e., pore spaces that contribute to fluid flow inside the formation (Rider, 2002). For that reason, effective porosity is what we aim to get in reservoir studies. We can determine ϕ_{eff} through basic petrophysical analysis using the neutron-porosity log and the density log. The GR log is also used to estimate the volume of shale (V_{sh}). This variable is required to convert total porosity (ϕ) into effective porosity by excluding isolated spaces and potential pore volumes where clay minerals may accommodate fluids.

Porosity values from two different logs (neutron-porosity and density) were used to estimate the RMS porosity, which is considered to be the total porosity. The effective porosity was then obtained through the following expression:

$$\phi_{eff} = \phi * (1 - V_{sh}) \tag{5-1}$$

The effective porosity was calculated for all the available wells. We then plotted these values against the log P-impedance to create a relationship between the two variables. This cross-plot is shown in Figure 5.27. Data points from four wells are used: Maari-1, Kea-1, Moki-1 and Whio-1. Since we want to predict the porosity at the reservoir zones, the cross-plot is constrained by the Gamma-Ray log to show just low GR values (sands). A polynomial curve was adjusted to the sand trend and it now correlates effective porosity and acoustic impedances through the following mathematical equation:

$$\phi_{eff} = -1.14x10^{-9}\mathrm{AI}^2 - 4.87x10^{-5}\mathrm{AI} + 0.495 \tag{5-2}$$

where ϕ_{eff} is the effective porosity in % and AI is the acoustic impedance in (m/s*g/cc).

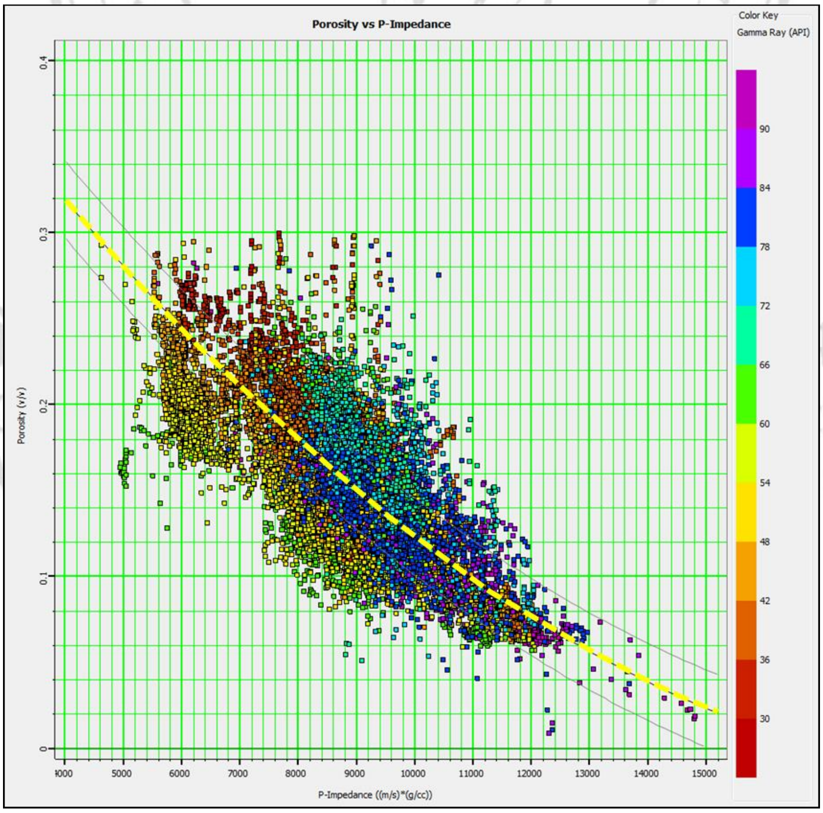

Figure 5.27: Effective porosity *vs.* computed P-Impedance values from wells Maari-1, Whio-1, Moki-1 and Kea-1

A detailed view of effective porosity within the Moki, Lower Manganui and Mangahewa formations along XL 1645 is shown in Figure 5.28. The colour ribbon shows the logged effective porosity along the Moki-1 well. The predicted effective porosity from the stochastic Gabor inversion is a good match within the Moki Fm. and a only moderate to decent match along the lower Manganui and Mangahewa. In the Moki Fm., effective porosity varies from 12 to 21%. Porosities are mostly overstimated in the lower Manganui section, which is expected since the created relationship was for the reservoir zones. Within the Mangahewa, most of the data in Moki-1 well shows porosities from 9 to 14%, except for thin intervals where it goes up to around 18%. The match between the inverted effective porosity and the logged effective porosity along the well is decent in the upper section of this formation, but only poor-to-moderate in the lower part.

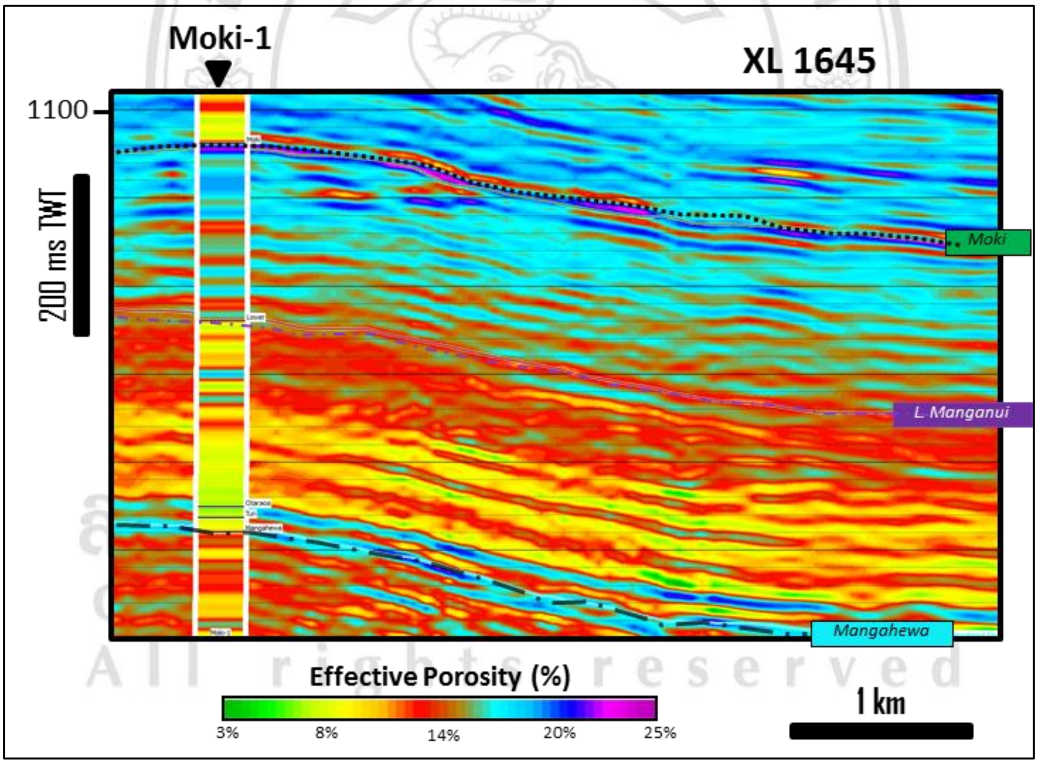

Figure 5.28: Inverted effective porosity from the stochastic Gabor Inversion along XL 1645. The color ribbon shows the logged effective porosity in the Moki-1 well

According to the Moki-1 completion report, two pay zones are found in the upper 20 meters of the Moki Fm., intervals 1306-1316 and 1317-1326 m MD below KB

(Figure 5.14). Table 5.1 presents the estimated petrophysical parameters for each of these zones (de Bock *et al.*, 1991). Figure 5.25a and b show in detail the stochastic Gabor inverted effective porosity around the Moki-Maari anticline at each pay zone. Search windows were used to extract average values. Zone 1 (a) used a search window of 8 ms below the Top Moki horizon and Zone 2 (b) used a search window of 6 ms below a phantom horizon 8 ms below the Top of Moki. Average inverted porosity around the crest of the Moki structure is 16.5 to 23.5% for Zone 1 (a) and 15.5 to 21% in Zone 2 (b). These values agree with what is shown in Table 5.1. Uncertainty (fluctuations) always will be present due to scatter data (see Figure 5.27). Very low inverted effective porosity values are associated to an artifact shown in Figure 5.18. These abnormal values are seen in both maps (a) and (b).

Table 5.1 – Petrophysical parameters of pay zones in Moki Fm., Moki-1 well

Interval (m MD)	Hydrocarbon Pay	Avg. Porosity	Avg. Sw
1306.1 - 1316.8	9.7 m	23.3%	24.2 %
1317.7 – 1326.2	7.3 m	19.4 %	33.7 %

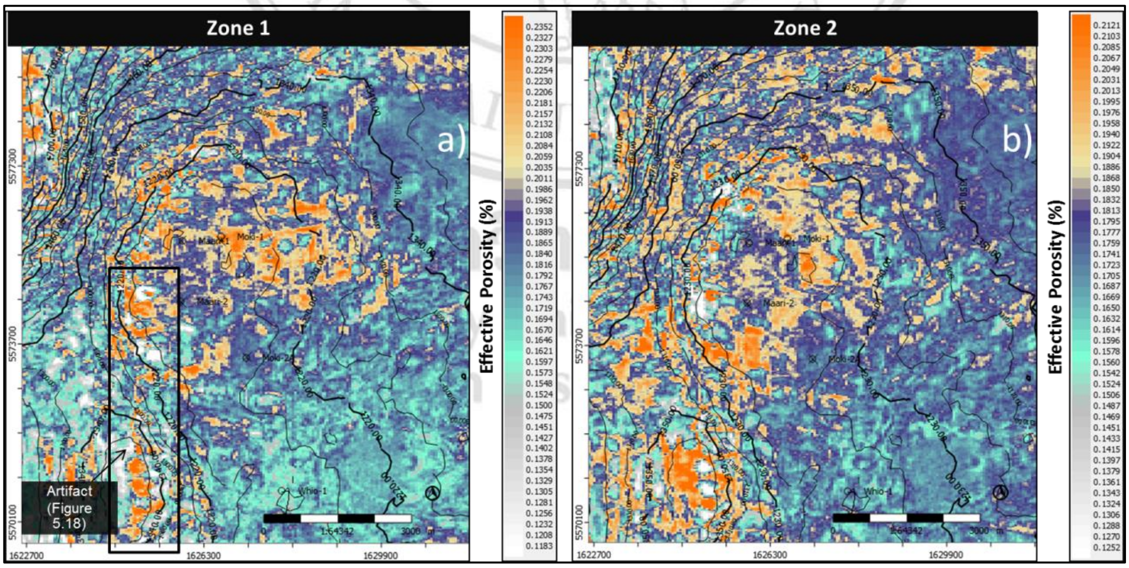

Figure 5.29: Inverted average ϕ_{eff} from two pay zones in the Moki formation. Zone 1 (a) is extracted with a search window of 8 ms below the Top Moki horizon and Zone 2 (b) used a search window of 6 ms below a phantom horizon 8 ms below the top of Moki formation. Structural contours are shown with a contour interval of 120 ms

Due to the depositional environment of the Moki formation deposits (submarine fans), lateral variations are expected, making it difficult to accurately predict porosity far from well control points. An example is seen in Figure 5.30. The plot shows P-Impedance *vs*. logged effective porosity in the Moki Fm. in two different wells: Moki-1 and Maui-4. Two trends are identified. Moki-1 follows the trend shown in Figure 5.27 and the Maui-4 presents a different trend with – in general – lower porosities for the same impedance value. The effective porosity histogram clearly shows a bimodal distribution (Figure 5.31). Hence a new relationship for the Moki formation in the Manaia structure is needed. A GR constraint was used to adjust a regression fit only to sands - low GR values – of the Moki Fm. (Figure 5.31). The mathematical expression relating acoustic impedance (m/s)*(g/cc) and effective porosity (%) for the sands in the Moki Fm. around the Maui-4 well is the following:

$$\phi_{eff} = -1.62x10^{-9}\mathrm{AI}^2 - 6.14x10^{-4}\mathrm{AI} + 0.51 \tag{5-3}$$

Inverted P-Impedance, stochastic Gabor inverted effective porosity and seismic data along the Moki formation in the Moki Fm. near the Maui-4 well are shown in Figure 5.32. The Gamma-Ray log is displayed along the seismic data, whilst the color ribbons represent the inversion property being shown. By using the new relationship (Equation 5-3), we obtained a fairly good match between logged (in Maui-4) and inverted porosities. In the lower part of the Moki section (below 1180 ms TWT), the match is decent as it differentiates layers with high and low porosities. In low porosity layers, which are normally associated with higher GR values (shale/sandy shales), the inverted porosity is normally overestimated by 3 or 4%. Remember, however, that Equation 5-3 was fit to a sand trend. In the upper section of the Moki Fm. (above 1180 ms TWT), the sands present a good match with the highest effective porosity (around 15%) in the first sand body of the formation (1115ms TWT). A thick sand package highlighted in Figure 5.32 (1140 to 1190 ms TWT) shows a good match between inverted and effective porosity from well data. Above that, inverted and calculated porosity values match very poorly, coinciding with a shale layer (1130 ms TWT).

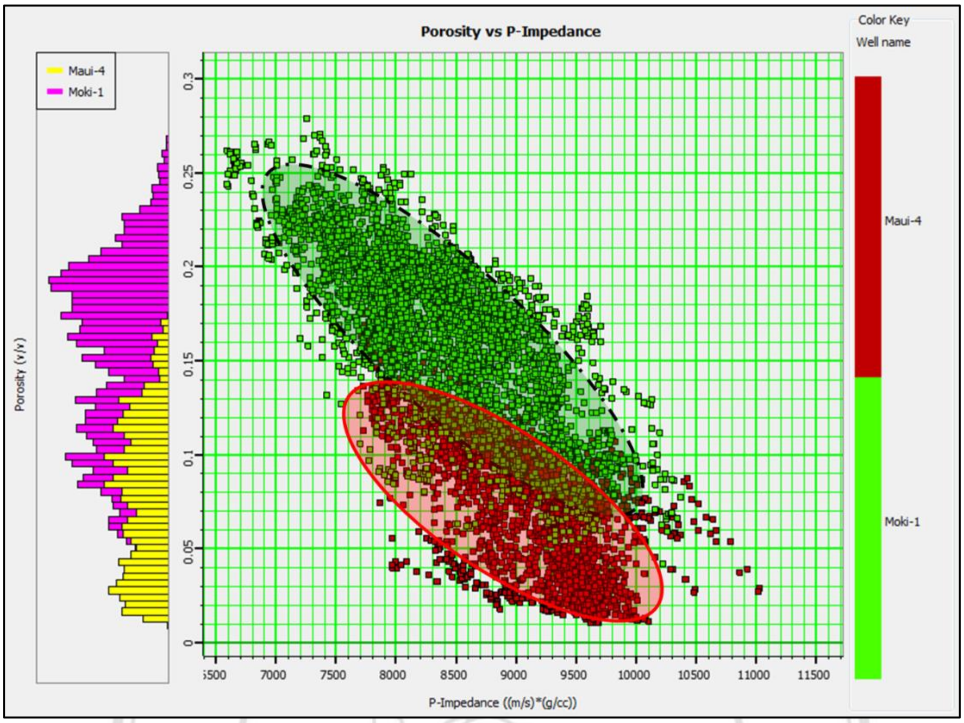

Figure 5.30: P-Impedance *vs.* effective porosity within the Moki Fm. in two different wells, one located in the Manaia anticline (Maui-4) and other in the Moki-Maari structure (Moki-1)

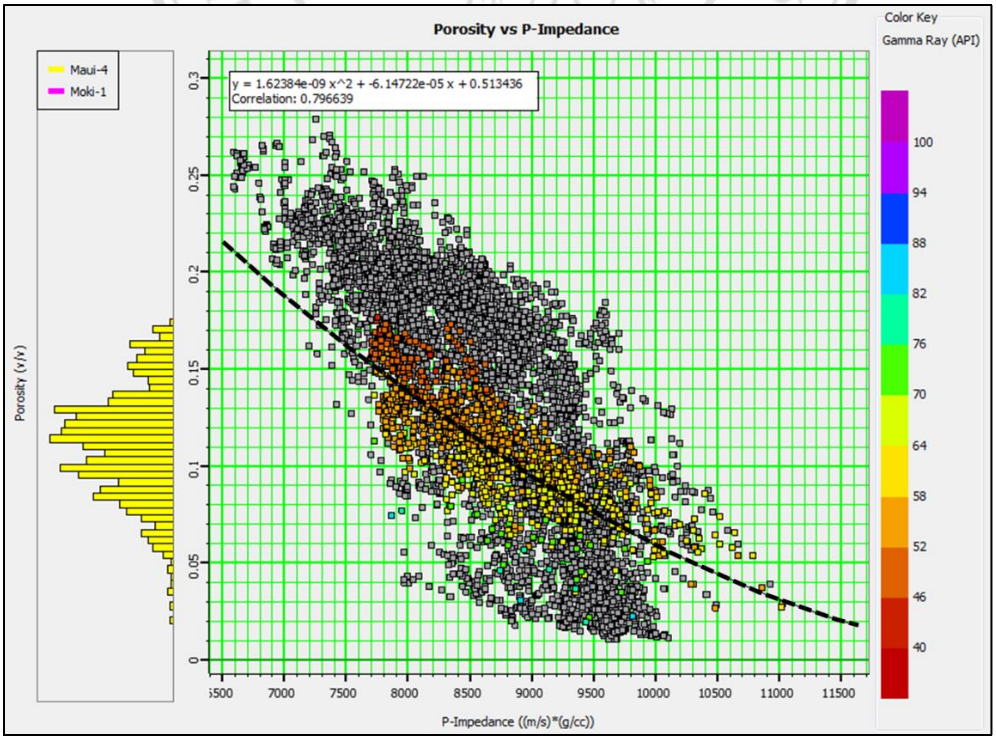

Figure 5.31: Cross-plot used to define a relationship between AI and effective porosity for sands of the Moki Fm. in the Manaia structure from the Maui-4 well data

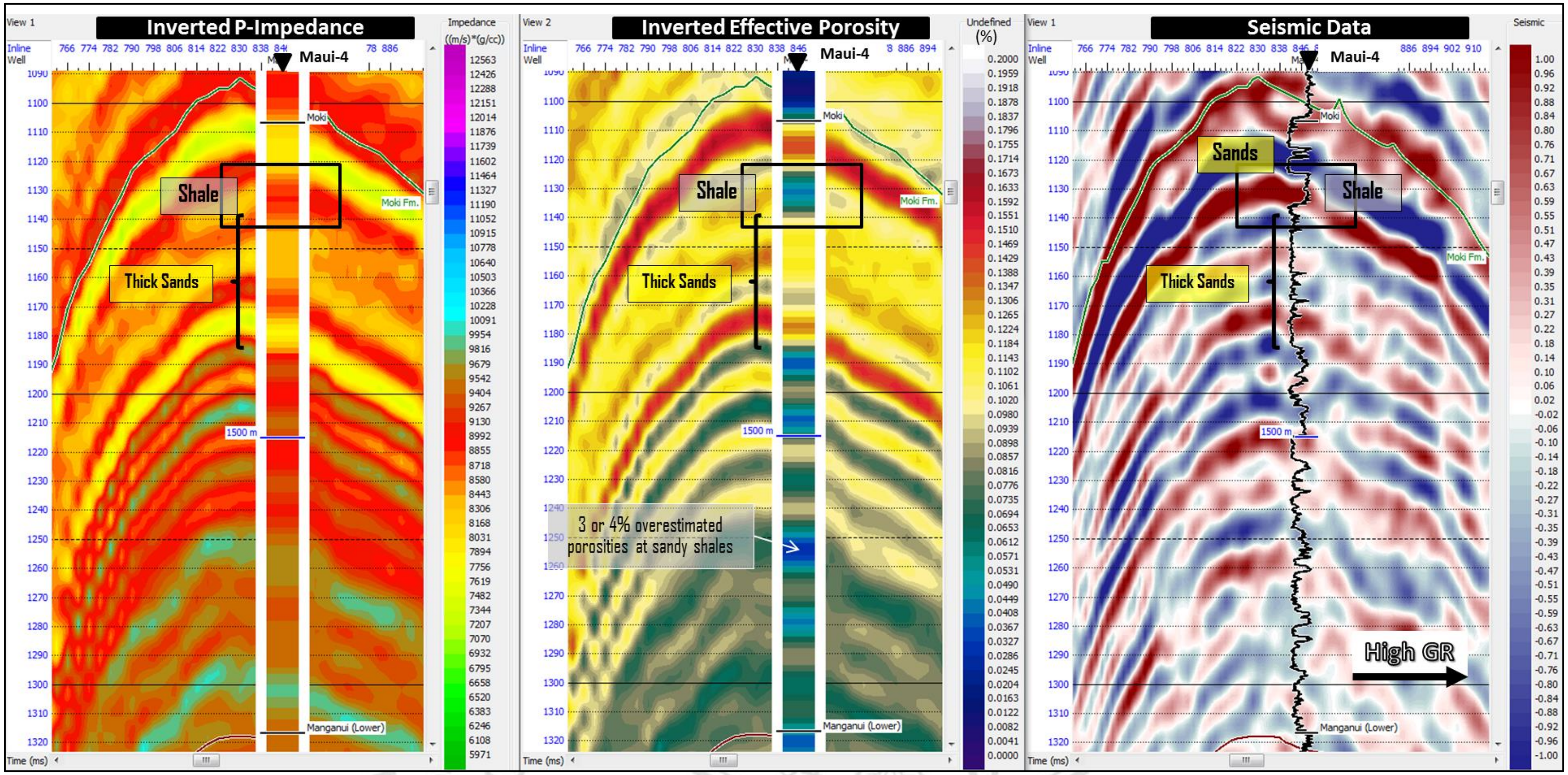

Figure 5-32: Inverted P-Impedance (left) and inverted effective porosity (middle) from stochastic Gabor inversion and seismic data showing in detail the Moki Fm. around the Maui-4 well on the Manaia anticline

Regardinf the second inversion interval, a stratal-slice was taken to map lateral variations of a pay zone (Maui-4 well) in the interval 2030-2041.8 m MD below KB, that on test flowed 575 bopd. The well completion report states the following petrophysical parameters for this zone:

Table 5.2 – Petrophysical parameters of a pay zones in Mangahewa Fm., Maui-4 well

Interval (m MD)	Hydrocarbon Pay	Avg. Porosity	Avg. Sw
2030-2041.8	11.8 m	12.8%	38%

Figure 5.33 shows the inverted average effective porosity (Eq. 5-2) from the referred pay zone. A search window of 6 ms below the Top Mangahewa horizon was used. Average ϕ_{eff} values around the Manaia strucure vary from 10% (gray color) to 15% (blue), approximately. These values match with the obtained from petrophysical analysis along the interval (Table 5.2). The predicted effective porosity is overall higher in the Moki-Maari structure, around 14-18%.

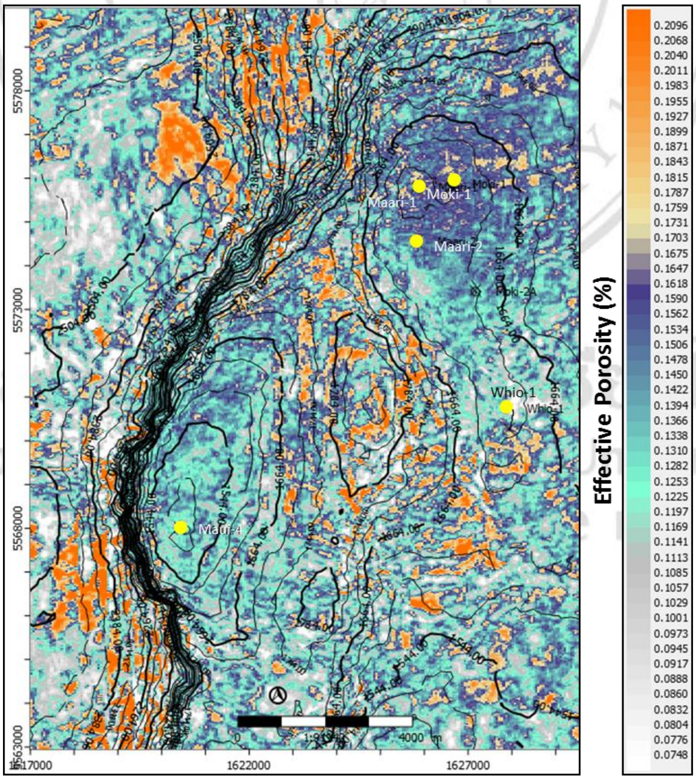

Figure 5-33: Inverted (stochastic Gabor) effective porosity values extracted from the upper 6 ms of the Mangahewa formation (HC pay zone). The average ϕ_{eff} was extracted along the pay interval. Structural contours (120 ms spacing) are also displayed